SENSITIVITY OF AEROSOL RADIATIVE EFFECTS TO SHIPPING EMISSIONS

by

Deanna Kerry

Submitted in partial fulfillment of the requirements
for the degree of Master of Science

at

Dalhousie University
Halifax, Nova Scotia
July 2019

Table of Contents

List of Tables iv

List of Figures v

Abstract vii

List of Abbreviations and Symbols Used viii

Acknowledgements xii

1 Introduction 1
- 1.1 Anthropogenic Climate Forcing . . . 1
- 1.2 Global Shipping . . . 3
  - 1.2.1 Sulfur Restrictions . . . 4
  - 1.2.2 Radiative Effects of Shipping Emission Restrictions . . . 5

2 Background and Theory 6
- 2.1 Aerosols . . . 6
  - 2.1.1 Aerosols and Humans . . . 6
  - 2.1.2 Aerosols and Climate . . . 7
  - 2.1.3 Sulfur Dioxide and Sulfate Aerosols . . . 16
  - 2.1.4 Black Carbon . . . 18
  - 2.1.5 Organic Carbon . . . 20
- 2.2 Ship Emissions . . . 20
  - 2.2.1 Sulfur Emissions and Restrictions . . . 21
  - 2.2.2 Black Carbon Emissions . . . 22
  - 2.2.3 Organic Carbon Emissions . . . 23
  - 2.2.4 Relationships Between Black Carbon, Organic Carbon, and Sulfate . . . 23

3 Model and Methods 25
- 3.1 The Continuity Equation . . . 25
- 3.2 GEOS-Chem . . . 26
  - 3.2.1 Model Chemistry . . . 27
  - 3.2.2 HEMCO and Emission Inventories . . . 27
  - 3.2.3 TOMAS . . . 28
  - 3.2.4 RRTMG . . . 30

3.2.5 GEOS-Chem runs conducted 32

4 Results and Discussion **33**
4.1 Sulfur dioxide 33
4.2 Black and organic carbon 39
4.2.1 Carbon Dioxide 44

5 Conclusions **46**

Bibliography **48**

List of Tables

1.1 AIS-registered ships in 2016 3
1.2 Sulfur limits for fuel in SECAs 4
1.3 Sulfur limits for fuel in other sea areas 4

3.1 HEMCO species of interest used 28

4.1 Simulations run 33
4.2 Summary of radiative effects of shipping emission scenarios. The scenario with the least warming relative to BAU is the IMO + BC restriction scenario. 45
4.3 Reduction in CO_2 required to make each shipping scenario climate-neutral 45

List of Figures

1.1 Globally averaged combined land and ocean surface temperature anomaly 2
1.2 Radiative Forcing Caused by Human Activities Since 1750s (EPA.gov) 2
1.3 Global ECAs and proposed ECAs 4

3.1 DRE calculations 31
3.2 AIE calculations 32

4.1 SO_2 and SO_4^{2-} concentrations in the BAU scenario 34
(a) SO_2 emissions in the 'BAU' scenario. 34
(b) SO_4^{2-} emissions in the 'BAU' scenario. 34
4.2 Radiative effects of 'BAU' scenario. The total radiative effects from shipping emissions in this scenario is -64.4 mWm^{-2} 35
(a) DRE due to the 'BAU' scenario. The global mean is -33.3 mWm^{-2} 35
(b) AIE due to the ''BAU' scenario. The global mean is -31.1 mWm^{-2}. 35
4.3 Change in SO_2 and SO_4^{2-} concentrations in the IMO scenario 36
(a) Change in SO_2 concentrations due to the IMO scenario. The global mean reduction in concentration is 0.0398 $\mu g/m^3$. . . . 36
(b) Change in SO_4^{2-} concentrations due to the IMO scenario. The global mean reduction in concentration is 0.0584 $\mu g/m^3$ . . . 36
4.4 Radiative effects of shipping emissions in the IMO scenario. The global mean radiative effects of this scenario is -19.1 mWm^{-2}. This is a warming of 45.3 mWm^{-2} compared to BAU. 38
(a) Change in shipping DRE due to the IMO scenario. The global mean change is 28.8 mWm^{-2}. DRE from shipping in this scenario is -4.5 mWm^{-2}. 38
(b) Change in shipping AIE due to the IMO scenario. The global mean is change 16.5 mWm^{-2}. AIE from shipping in this scenario is -14.6 mWm^{-2}. 38
4.5 BC and OC concentrations in the BAU scenario 39
(a) BC concentrations in the 'BAU' scenario. 39
(b) BC and OC concentrations in the 'BAU' scenario. 39
4.6 Change in BC and OC concentrations in the 'BC restriction' and 'BC and OC restriction' scenarios 41

(a) Change in BC emissions in the 'BC restriction' scenario. The global mean reduction is 0.0017 $\mu g/m^3$. 41
(b) Change in BC and OC emissions in the 'BC and OC restriction' scenario. The global mean reduction is 0.0029. $\mu g/m^3$. 41
4.7 Change in shipping DRE due to 'BC restriction' scenario for external and internal mixing 42
(a) Change in shipping DRE due to the 'BC restriction' scenario with external mixing assumed. The global mean is -0.766 mWm^{-2} 42
(b) Change in shipping DRE due to the 'BC restriction' scenario with internal mixing assumed. The global mean is -1.30 mWm^{-2} 42
4.8 Change in shipping DRE due to 'BC restriction' scenario for external and internal mixing 43
(a) Change in shipping DRE due to the 'BC and OC restriction' scenario with external mixing assumed. The global mean is -0.581 mWm^{-2} 43
(b) Change in shipping DRE due to the 'BC and OC restriction' scenario with internal mixing assumed. The global mean is -1.10 mWm^{-2} 43
4.9 Change in shipping AIE due to the 'BC + OC restriction' scenario. The global mean is 9.60 mWm^{-2} 44

Abstract

In 2020, The International Maritime Organization (IMO) will enforce significant restrictions on SO_2 emissions from global shipping to improve public health. SO_2 forms SO_4^{2-} aerosols, which have a cooling effect on climate. A reduction in SO_4^{2-} leads to atmospheric warming. In order to explore making this policy climate-neutral, we investigated the sensitivity of radiative forcing to potential restrictions on black carbon (BC) emissions. BC emissions are also closely tied to organic carbon (OC) emissions: reductions of one often leads to reductions of the other.

The direct and indirect radiative effects from SO_4^{2-}, BC, and OC aerosols emitted by ships were calculated using the chemical transport model GEOS-Chem. The TwO-Moment Aerosol Sectional (TOMAS) module was used to calculate particle number and mass of shipping aerosols, and the Rapid Radiative Transfer Model for General Circulation Models (RRTMG) module was then used to calculate the radiative fluxes at the top of the atmosphere. Simulations were performed for the year 2013 with 1-month December 2012 spinup. We investigated 4 different scenarios: the 'business-as-usual' (BAU) scenario with no changes to emissions, an 'IMO' scenario with 85% less SO_2 emissions from ships, an 'IMO + BC reduction' scenario with 85% less BC and SO_2 emissions from ships, and an 'IMO + BC + OC' reduction scenario, with 85% less BC, OC, and SO_2.

It was determined that the IMO scenario leads to a global average of 45.3 mWm^{-2} of increased warming compared to the BAU scenario. The 'IMO + BC reduction' leads to 44.0 - 44.5 mWm^{-2} of increased warming, suggesting that a BC reduction is not sufficient to offset the warming from the 2020 SO_2 restrictions. The 'IMO + BC + OC' scenario leads to 53.8 - 54.3 mWm^{-2} of increased warming. This is even larger than the warming introduced by the 'IMO' scenario and is an undesirable scenario from a climate perspective. In order to make each scenario climate-neutral, CO_2 from ships would have to be reduced by 47 to 65% on a 100-year timescale.

List of Abbreviations and Symbols Used

$\bar{\omega}$	Single scattering albedo
ν	Wavelength
ρ_L	Density of a liquid
σ	Cross section
τ	Optical thickness
$\nabla \cdot F$	Flux divergence
A	Albedo
a	Absorption
A_c	Vertically projected cloud fraction
e	Extinction
F	Flux
F_{clear}	Flux through clear atmosphere
F_{cloudy}	Flux through cloudy atmosphere
$f_{\nu,j}$	Normalized line shape
$g(k)$	Cumulative probability function
h	Height within a cloud
$h(k)$	Wavenumber domain at k
I	Intensity of radiation
k_ν	Absorption coefficient
L	Loss
L^{-1}	Inverse Laplace transform
L_a	Length over which absorption takes place

N	Particle number density
$n(r)$	Number concentration of droplets of radius r
$n(X,t)$	Number density
P	Production
p	Pressure
Q	Extinction efficiency
r	Radius
s	Scattering
$S_j(T)$	Line intensity
T	Temperature
T_ν	Transmittance
u	Path length
V	Volume
W	Liquid water content
z	Height
AGWP	Absolute Global Warming Potential
AIE	Aerosol indirect effect
AIS	Automatic Identification System
AOD	Aerosol optical depth
ARCTAS	Arctic Research of the Composition of the Troposphere from Aircraft and Satellites
BAU	Business as usual
BC	Black carbon
CCN	Cloud condensation nuclei
CDNC	Cloud droplet number concentration
CEDS	Community Emissions Data System
CKD	Correlated k-distribution

CTM	Chemical Transport Model
DRE	Direct radiative effect
ECA	Emission Control Area
EC	Elemental carbon
EPA	Environmental Protection Agency
GADS	Global Aerosol Dataset
GC	GEOS-Chem; Goddard Earth Observing System Chemical Transport Model
GEOS-Chem	Goddard Earth Observing System Chemical Transport Model
GEOS-FP	GEOS Forward Processing meteorological data
GMAO	Global Modelling and Assimilation Office
HEMCO	Harvard-NASA Emissions Component
ICA	Independent Column Approximation
IMO	International Maritime Organization
LBLRTM	Line-by-line radiative transfer model
McICA	Monte Carlo Independent Column Approximation
NASA	National Aeronautics and Space Administration
NMVOC	Non-methane volatile organic compound
OC	Organic carbon
$PM_{2.5}$	Particulate matter with diameter < 2.5 μm
RRTMG	Rapid Radiative Transfer Model for General Circulation Models
SECA	Sulfur Emission Control Area
SO_2	Sulfur dioxide
SO_4^{2-}	Sulfate
SOA	Secondary organic aerosol
SSA	Single scattering approximation
TOMAS	TwO-Moment Aerosol Sectional

TSA	Two-stream approximation
UN	United Nations
VOC	Volatile organic compound
WHO	World Health Organization
H_2O_2	Hydrogen peroxide
H_2SO_4	Sulfuric acid
HO_2	Hydroperoxyl
HSO_3	Hydrogen sulfite
M	Chemical third body
NO_x	Nitrogen oxides: NO, NO_2
O_x	Oxides: O, O_3
OH	Hydroxide
SO_3	Sulfur trioxide

Acknowledgements

This thesis is dedicated to Patrick Strongman.

I would like to thank Dr. Randall Martin for his guidance and enthusiasm in supervising my project over the last two years. He listened carefully to my interests and helped me work on a topic that combined my interests in atmospheric science and public policy. I am very grateful to be a part of his research group here at Dalhousie.

I would also like to thank the rest of Atmospheric Composition Analysis Group, especially Betty Croft, Melanie Hammer, Jun Meng, and Colin Lee for their help in fixing technical problems and providing valuable scripts to help complete my research. Additionally, I would like to thank Dr. Jeffrey Pierce and Dr. Kelsey Bilsback of Colorado State University for helping me overcome the final hurdle in running the last simulations I needed to complete my project. I cannot overstate how important this assistance was.

Finally, I would like to thank the GEOS-Chem Support Team for their amazing support and timely responses to all of my questions about running GEOS-Chem simulations.

Chapter 1

Introduction

1.1 Anthropogenic Climate Forcing

Since the mid-19th century during the industrial revolution, humans have been contributing to changes in the Earth's climate by emitting greenhouse gases and particulate matter (aerosols) into the atmosphere. As greenhouse gas emissions increase due to human activity, more infrared radiation from the earth is absorbed by these gas molecules. This reduces the outgoing radiation at the top of the atmosphere. As a result, surface temperatures increase to maintain a global radiative equilibrium. Anthropogenic greenhouse gas emissions have continued to rise in recent history, leading to a rise in global surface temperatures over the last century. This warming is illustrated by Figure 1.1 (Pachauri and Meyer, 2014). Carbon dioxide, methane, and nitrous oxide are the most significant anthropogenic greenhouse gases emitted through power generation, agriculture and land use, and waste management (Houghton, 2015).

Aerosols contribute to radiative changes directly by absorbing and scattering solar radiation. This is known as the 'direct radiative effect' (DRE), the instantaneous radiative impact of aerosols on the Earth's energy balance (Heald et al., 2014). Aerosols also contribute to radiative changes indirectly by altering the albedo and lifetime of clouds, which affects how much solar radiation is scattered. This is the 'aerosol indirect effect' (AIE).

With the exception of the dark and absorbing black carbon aerosol, most aerosols

Figure 1.1: Globally averaged combined land and ocean surface temperature anomaly

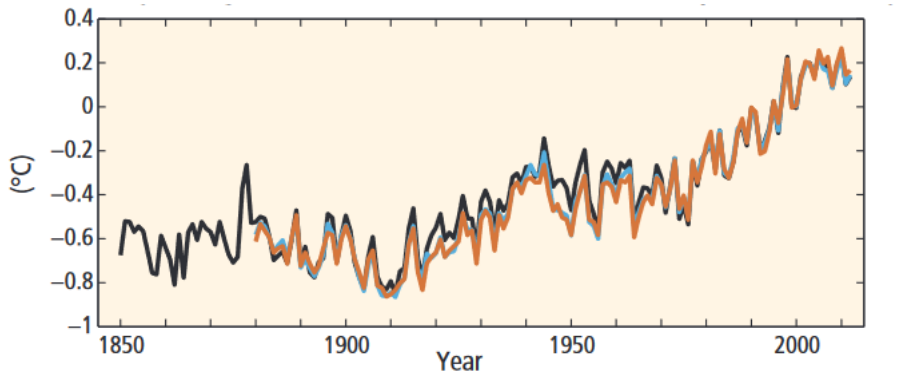

cool the atmosphere through direct and indirect effects. This cooling effect reduces the impact of warming due to greenhouse gases. The radiative forcings of aerosols and greenhouse gases are compared in Figure 1.2 (US EPA, 2014).

Figure 1.2: Radiative Forcing Caused by Human Activities Since 1750s (EPA.gov)

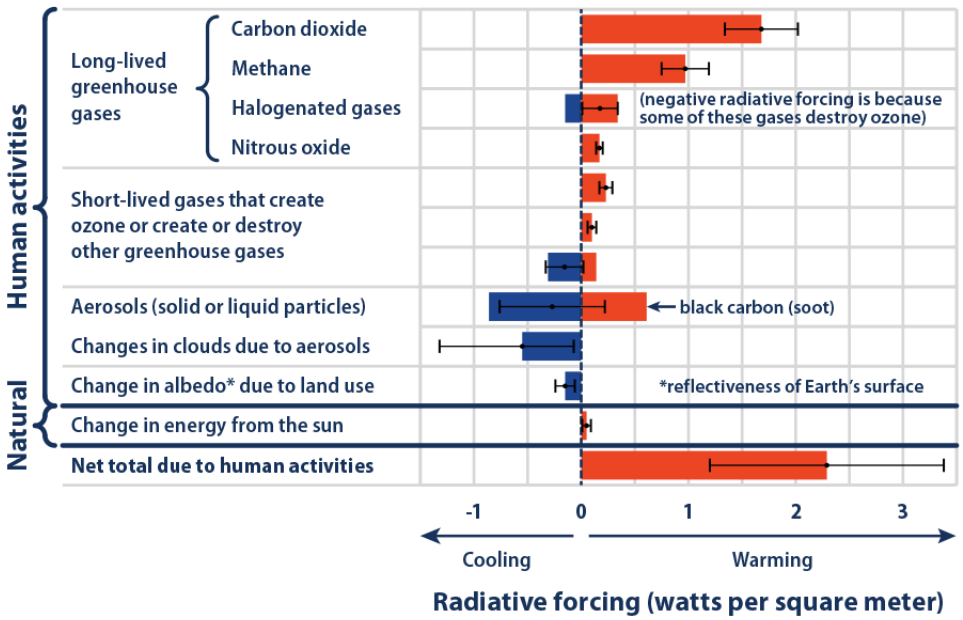

One example of these species is sulfate (SO_4^{2-}), which cools the atmosphere through the direct and indirect effect. These aerosols are emitted naturally from bacteria and volcanoes, and through anthropogenic mechanisms such as fossil fuel burning. A notable source of sulfate aerosols is the shipping industry. Ships release sulfur dioxide

into the atmosphere when fuel containing sulfur is burned. This sulfur dioxide can be converted to sulfate aerosols through the processes described in Section 2.1.3. Ships are also a significant source of black carbon, which warms the atmosphere through the direct effect.

1.2 Global Shipping

Shipping has been a significant method of transportation and trade throughout human history. This ability to efficiently move large amounts of goods and materials long distances is unmatched by any other form of transportation. Today, over 90% of global shipping trade weight is transported around the world by ships (UN-Business Action Hub). Table 1.1 lists the marine vessels were registered with the IMO automatic identification system (AIS) in 2016.

Bulk carriers	778,890
General cargo (multipurpose ships)	75,258
Oil tankers	503,343
Container ships	244,274
Chemical tankers	44,347
Ferry/passenger ships	5950
Liquified natural gas (LNG) tankers	1800
Total	**1,806,650**

Table 1.1: AIS-registered ships in 2016

This massive global industry is responsible for many greenhouse gas and aerosol emissions, including sulfur dioxide. Although sulfur dioxide emissions lead to increased atmospheric cooling, sulfur dioxide gas and sulfate aerosols cause a number of human health problems. Due to these undesired health effects, sulfur restrictions have been imposed on the shipping industry.

1.2.1 Sulfur Restrictions

The most comprehensive restrictions on shipping emissions were created by the International Maritime Organization. These restrictions govern global waters and several special coastal areas called "Emission Control Areas" (ECAs). A map of these ECAs is shown in Figure 1.3, taken from Fagerholt et al. 2015.

Figure 1.3: Global ECAs and proposed ECAs

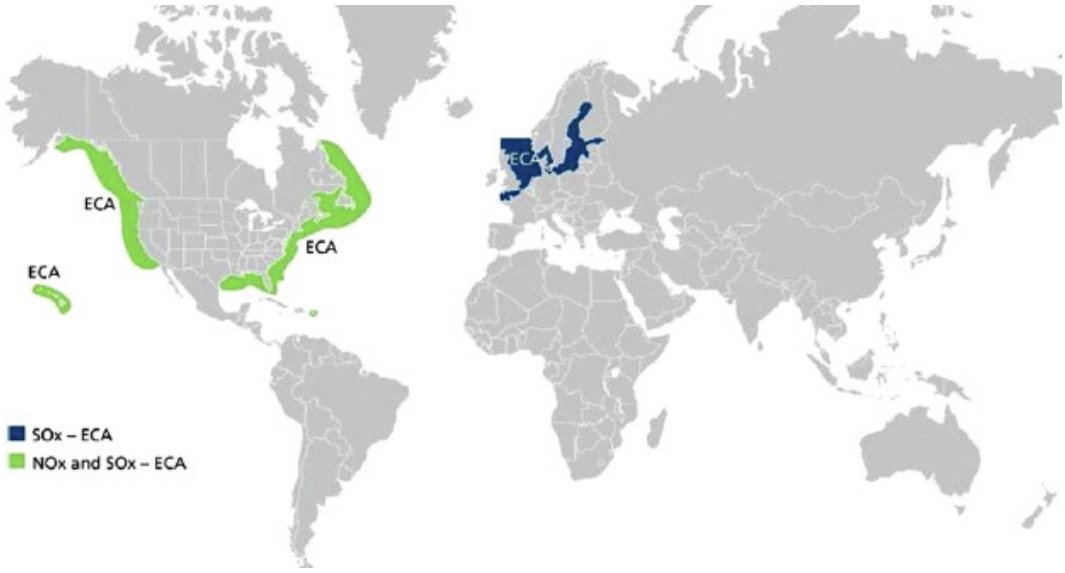

Sulfur ECAs (SECAs) describe restrictions on sulfur content in ship fuel to reduce sulfur oxide (SO_x) emissions. These restrictions are quantified in Table 1.2 and Table 1.3.

Table 1.2: Sulfur limits for fuel in SECAs

before 1 July 2010 (starting in 2007)	1.50% m/m
between 1 July 2010 and 1 January 2015	1.00% m/m
after 1 January 2015	0.10% m/m

Table 1.3: Sulfur limits for fuel in other sea areas

before 1 January 2012	4.50% m/m
between 1 January 2012 and 1 January 2020	3.50% m/m
after 1 January 2020 (may be changed to 2025)	0.50% m/m

By January 2020, the sulfur content limit decreases by 85-90% worldwide. To achieve this goal, ship owners must rely on exhaust cleaning systems, start using liquefied natural gas as fuel, or implement other technologies (Walker et al., 2018). Many proposed solutions have negative environmental or financial consequences; a common solution has not adopted by all ship owners at the current time.

1.2.2 Radiative Effects of Shipping Emission Restrictions

Recent research estimates that the 2020 sulfur restrictions will lead to an overall reduction in atmospheric cooling of approximately 71 mWm^{-2} due to reduced atmospheric sulfate concentrations (Sofiev et al., 2018). While likely to lead to better health outcomes for coastal populations, these restrictions are problematic from a climate perspective: warming the atmosphere leads to rising sea levels and increased human exposure to extreme heat waves (Dosio et al., 2018). In order to offset this warming and allow and shift the policy outcomes to become climate-neutral, other shipping emissions will have to be reduced along with sulfur dioxide to create a negative radiative effect. Black carbon has not been regulated in the shipping industry, despite the fact that up to 2% of global black carbon aerosols may originate from ships (International Maritime Organization, 2015). Due to current lack of regulations, this project explores the radiative effects that result from black carbon reductions.

Chapter 2

Background and Theory

2.1 Aerosols

2.1.1 Aerosols and Humans

Aerosols are small particles suspended in the atmosphere ranging in size from less than 0.01 μm to 10 μm in diameter (Jacob, 1999). Aerosols are classified as primary aerosols or secondary aerosols. Primary aerosols are emitted directly from a source through mechanical action, such as sea salt emission from ocean waves, or wind-driven dust suspension in the atmosphere. Secondary aerosols are formed through a chemical reaction in the atmosphere that may take place on the surface of another aerosol. For example, aerosols are produced through the combustion of fossil fuels when nitrogen oxides undergo several chemical processes to form nitrate aerosols (Tomasi et al., 2017). Both primary and secondary aerosols have a wide range of effects on human health, ocean chemistry, and climate change.

Aerosols affect human health in several ways that depend on their size and composition. Particles smaller than 10μm are considered to have greater impact on human health than larger particles because they are less effectively trapped in nasal mucus and cilia and are more likely to enter the lungs. As particle size decreases, particles can penetrate deeper into the body though the lungs and ultimately into the circulatory system via the alveoli (Löndahl et al., 2007). Aerosols that enter the lungs

and circulatory system cause many health problems: respiratory, cardiovascular, and blood disorders have all been linked to exposure to ambient particulate matter (Kim et al., 2015). Particulate matter has also been classified as a Group I carcinogen by the International Agency for Research on Cancer, meaning enough evidence exists to link particulate matter to cancer (Hamra et al., 2014). According to the World Health Organization (WHO), exposure to particulate matter smaller than 2.5 μm in diameter ($PM_{2.5}$) caused 4.2 million premature deaths worldwide in 2016 (World Health Organization, 2018). A premature death occurs before the average age of death in a given population. In order to limit death and disease caused by PM, WHO has created air quality guidelines for coarse and fine particulate matter (World Health Organization, 2018).

2.1.2 Aerosols and Climate

Direct Effect

Aerosols cause changes in global temperatures by absorbing or reflecting solar (shortwave) and terrestrial (longwave) radiation. This direct interaction with light is called the direct radiative effect (DRE). Aerosol properties such as shape and composition determine whether the light is scattered or absorbed. The sum of absorption and scattering is known as 'extinction':

$$\text{Extinction (e)} = \text{absorption (a)} + \text{scattering (s)}$$

These quantities are unitless numbers between 0 and 1. If all light passing through a substance is absorbed or scattered, e = 1. It is also useful to define the single scattering albedo (SSA) , $\bar{\omega}$

$$\bar{\omega} = \frac{s}{a+s} \tag{2.1}$$

For highly reflective aerosols, $\bar{\omega}$ will be close to 1. In constrast, dark and highly absorbing aerosols will have a small $\bar{\omega}$ (Chance and Martin, 2017). Most anthro-

pogenic aerosols have a $\bar{\omega}$ value close to 1 (with the notable exception of black carbon aerosols), leading to an overall global cooling effect. A 2014 study using GEOS-Chem with a radiative transfer model (RRTMG) estimated that all anthropogenic aerosols were responsible for -0.36 Wm^{-2} of global cooling in 2010 (Heald et al., 2014).

Both scattering and absorption are also described by cross-sections, σ_s and σ_a. Atmospheric cross-section differs from the standard geometric definition and instead refers to the intensity of the radiation scattered or absorbed. The cross-section is an inherent property of the material (Jacob, 1999). From this, we can define the optical thickness, τ, a dimensionless quantity that is useful for describing extinction:

$$\tau_e = \int_0^{L_a} \sigma_e N dl \tag{2.2}$$

Where L_a is the length over which absorption or scattering takes places, and N is the number density of particles (Chance and Martin, 2017). As τ_e increases, the number of photons scattered or absorbed increases, meaning greater extinction has occurred. τ_e is wavelength-dependent and is also referred to as 'aerosol optical depth' (AOD). AOD is often calculated using $\tau = k_\nu u$, where k_ν is the absorption coefficient, which quantifies how far into a material radiation may penetrate before being absorbed, and u is the path length of the radiation. We use the AOD to determine the intensity of light [$\mathrm{Wm}^{-2}\mathrm{sr}^{-1}(\mathrm{cm}^{-1})^{-1}$] passing through the atmosphere through the Beer-Lambert law:

$$I(\nu) = I_0 e^{-\tau(\nu)} \tag{2.3}$$

Where ν is the wavenumber of the radiation. The intensity of radiation decreases with increasing AOD. Intensity is closely related to the transmittance, T, which describes how much light passes through a substance:

$$T(u) = \frac{1}{\Delta\nu}\int_{\Delta\nu} e^{-\tau} d\nu = \frac{1}{\Delta\nu}\int_{\Delta\nu} e^{-k_\nu u} d\nu \tag{2.4}$$

For a given wavenumber and species, multiple absorption lines can contribute to the transmittance, so the total optical depth becomes a sum of optical depths. This can be described using a discrete summation or, more completely, a continuous integration:

$$\tau = \sum_{j=1}^{N} \tau_j = \int_u \sum_{j=1}^{N} k_{\nu,j}(u)du \tag{2.5}$$

k_ν is the product of the line intensity, S_j and the normalized line shape, $f_{\nu,j}$

$$k(\nu, p, T) = \sum_i S_j(T) f_{\nu,j}(\nu, p, T) \tag{2.6}$$

The line intensity is dependent on temperature, and the line shape is dependent on both temperature and pressure (Fu and Liou, 1992)(Box and Box, 2016). Calculating the transmittance requires knowing the k_ν. In practice, this is often very difficult.

K-distribution method

The more complex (i.e. non-gray) models of the atmosphere require consideration of many absorption spectral lines. This means the wavelength increments used when calculating equation 2.4 analytically must very small. In practice, this large number of integrations for each spectral line ('line-by-line") is extremely computationally expensive (Fu and Liou, 1992). Approximations must therefore be made to reduce the number of integrations performed. One of the many approximations available is the k-distribution method. This method assumes a homogenous atmosphere with constant temperature and pressure in which only k varies within a defined spectral interval, even if k is actually a function of wavenumber. Let $h(k)dk$ be part of the wavenumber domain between k and $k + dk$. We may then rewrite equation 2.4 as an integral over k instead of ν:

$$T_\nu(u) = \frac{1}{\Delta\nu} \int_{\Delta\nu} e^{-k_\nu u} d\nu = \int e^{-ku} h(k)dk \tag{2.7}$$

This is the k-distribution approach. It replaces a detailed line structure with a smooth function that is easier to integrate. The limits on 2.7 may be a particular range of absorption coefficients, or left from 0 to infinity. Equation 2.7 is much more easily integrated than equation 2.4, reducing computation time. It is also the inverse Laplace transform of T:

$$h(k) = L^{-1}[T_\nu(u)] \tag{2.8}$$

An analytical expression for $h(k)$ may be derived if T can be expressed in terms of an analytical exponential function and if the Laplace transform (equation 2.8) can be performed (Fu and Liou, 1992)(Box and Box, 2016). We can also write a cumulative probability function:

$$g(k) = \int_0^k h(k')dk' \tag{2.9}$$

where $g(0) = 0$ and $g(k \to \infty)$. $g(k)$ is smooth and monotonically increasing in k-space. The spectral transmittance is now:

$$T_\nu = \int_0^1 e^{-k(g)u}dg \approx \sum_{j=1}^{J} e^{-k(g_j)u}\Delta g_j \tag{2.10}$$

$k(g)$ will also be a smooth function in g-space. The difficult integration in equation 2.4 is now a finite sum, which can be computed much more easily. Approximately 5 – 10 terms are necessary for accurate results (Box and Box, 2016).

Correlated k-distribution

For longer path lengths, the homogeneous approximation becomes a poor model and nonhomogeneous atmospheres must be considered. In this case, the k-distribution method is insufficient because k_ν varies with pressure. If we consider a nonhomoge-

neous atmosphere between heights z_1 and z_2, the transmittance is

$$T_\nu = \int_{\Delta\nu} \exp\Big[- \int_{z_1}^{z_2} k(\nu, p, T)\rho dz \Big] \frac{d\nu}{\Delta\nu} \tag{2.11}$$

where ρ is the density of the absorber (Fu and Liou, 1992). In this scenario, we seek to find the conditions under which the transmittance can be described using a form similar to equation 2.10, where k is a function of g:

$$T_\nu = \int_0^1 \exp\Big[- \int_{z_1}^{z_2} k(g, p, T)\rho dz \Big] dg \tag{2.12}$$

This method for calculating the transmittance is called the correlated k-distribution (CKD). It assumes there exists only one value of g at different heights for a given value of ν (Fu and Liou, 1992). Deducing equation 2.12 from equation 2.11 requires a number of assumptions outlined in Fu and Liou 1992. The CKD model provides exact answers for single lines, periodic lines, and the weak and strong line limits. This model is used in radiative transfer calculations in the GEOS-Chem model, discussed further in the next chapter.

Monte Carlo Independent Column Approximation

In radiative transfer calculations, it is necessary to make approximations regarding the direction of propagated radiation. In many models, a multi-layer two-stream approximation (TSA) is used. The TSA assumes that each layer of the atmosphere is horizontally homogenous so that radiation in any given vertical column (model gridbox) does not interact with radiation in another vertical column. The CKD flux calculation within in an atmospheric column uses the TSA. It is a sum of the vertical

fluxes over the spectral intervals of interest:

$$F = \sum_{k=1}^{K} c_k F(j,k) \tag{2.13}$$

where K is the number of spectral intervals, j is the column of interest, and c_k is the absorption coefficients. The CKD assumes parallel-plan homogeneous atmosphere, meaning that horizontal homogeneity in cloud optical thickness in each column is assumed (Oreopoulos et al., 2007). However, this assumption is much too simplistic; clouds often have significant horizontal variability within a given column. To introduce horizontal variability in clouds, the independent column approximation (ICA) can be used to find the domain average fluxes over J smaller subcolumns. The vertical flux calculation within a column becomes

$$\langle F \rangle = \frac{1}{J} \sum_{k=1}^{K} \sum_{j=1}^{J} c_k F(j,k) \tag{2.14}$$

which can be divided into cloudy and clear summations

$$\langle F \rangle = (1 \breve{} A_c)\Big(\sum_{k=1}^{K} c_k F^{\text{clear}}(j,k)\Big) + A_c\Big(\frac{1}{J_c} \sum_{j=1}^{J_c} \sum_{k=1}^{K} c_k F^{cloudy}(j,k)\Big) \tag{2.15}$$

Here, A_c is the vertically projected cloud fraction (Pincus et al., 2003). This equation may be simplified to

$$\langle F \rangle = (1 \breve{} A_c) F_{clear} + A_c \langle F_{cloudy} \rangle \tag{2.16}$$

where F_{clear} is the flux through the clear atmosphere and $\langle F_{cloudy} \rangle$ is the domain-average flux through cloudy atmosphere. This method for calculating the domain-average flux is extremely accurate but very computationally expensive because the flux calculations are performed over spectral intervals for many different cloud states.

Its impracticality has led to the adoption of Monte Carlo methods as an alternative to the ICA. Monte Carlo methods rely on repeated random sampling of values that are accepted or rejected based on pre-defined criteria. The Monte Carlo Independent Column Approximation (McICA) produces randomly generated horizontal subcolumn optical properties during the spectral integration (Barker et al., 2008)(Pincus et al., 2003). Specifically, $\langle F_{cloudy} \rangle$ in equation 2.16 is replaced by $\sum_{k=1}^{K} c_k F^{cloudy}_{random\{1,\ldots,J_c\},k}$. In this term, the average flux through cloudy atmosphere in a subcolumn is randomly generated for each spectral interval of interest. Multiple integrations over all cloud states can be avoided, because the average value is generated and not directly calculated (Pincus et al., 2003). A subcolumn with a single, homogeneous cloud state will have identical results for ICA and McICA. The model in this project uses McICA routines.

Geographic distribution of aerosols

It is important to note that the overall aerosol cooling due to the direct effect does not simply cancel a portion of greenhouse gas warming (Brasseur et al., 1999). Most greenhouse gases in the troposphere are relatively well-mixed and have the strongest radiative effects within thirty degrees north and south of the equator. On the other hand, most anthropogenic aerosols are in the Northern Hemisphere and cause the most cooling in mid-latitudes. They are not as well-mixed as many greenhouse gases due to their much shorter atmospheric lifetime. The radiative forcing due to greenhouse gases and aerosols will change global temperature gradients, but these opposing effects will not cancel each other out on the local scale (Brasseur et al., 1999). Geographic distribution of aerosols remains an important consideration when studying their radiative effects.

First Indirect Effect

The formation of clouds requires aerosols to serve as cloud condensation nuclei (CCN). Water droplets condense on CCN and grow through condensation, collision, and coalescence (Feingold et al., 1996). Because of this relationship to clouds, aerosols contribute to radiative effects through their influence on cloud properties. One phenomenon by which aerosols affect clouds properties is through the first indirect effect, or the "Twomey Effect". This relates to the albedo (reflectivity) of clouds. In general, if we consider a cloud of optical thickness τ of height h with $n(r)$ droplets of radius r, we can write the relationship between these parameters as

$$\tau = \pi h \int_0^\infty Q_e r^2 n\left(r\right) dr \tag{2.17}$$

Where Q is the extinction efficiency. Optical depth depends on the thickness, droplet radius, and droplet concentration of the cloud. Within the visible range of the electromagnetic spectrum, Q $\approx$ 2. If we assume the droplets are similar in size and have the average radius of $\bar{r}$, we can write

$$\tau = 2\pi h \bar{r}^2 N \tag{2.18}$$

where N is the number concentration of droplets formed by cloud condensation nuclei (CCN):

$$N = \int_0^\infty n\left(r\right) dr \tag{2.19}$$

Calculation of N requires information about the size of the particles. The liquid water content, W, of the cloud is expressed as

$$W = \frac{4}{3}\pi \rho_L \left(\bar{r}\right)^3 N \tag{2.20}$$

Combining equations 2.18 and 2.20, we write

$$\tau = 2.4 \left(\frac{W}{\rho_L} \right)^{2/3} h N^{1/3} \tag{2.21}$$

Upon inspection we see that as the number concentration, N, increases, so too will the optical thickness of the cloud. This is the general theory of the Twomey effect.

If we hold W and h constant, we can differentiate and obtain

$$\frac{\Delta\tau}{\tau} = \frac{1}{3} \frac{\Delta N}{N} \tag{2.22}$$

The albedo of a cloud can be expressed by

$$A = \frac{(1-g)\,\tau}{1 + (1-g)\,\tau} \tag{2.23}$$

where g is the scattering asymmetry factor, a parameter useful for quantifying the average angle of reflection for a given type of particle. In the case of clouds made of water droplets, g $\approx$ 0.85 and the equation becomes

$$A \approx \frac{\tau}{\tau + 6.7} \tag{2.24}$$

Combining equations 2.22 and 2.24 , we see

$$\frac{\Delta A}{\Delta N} = \frac{A\,(1-A)}{3N} \tag{2.25}$$

(Hobbs, 1993). As Hobbs points out in his derivation, this equation can be used to show that anthropogenic aerosols increase cloud albedo most effectively in locations with relatively few aerosols, primarily remote locations and over oceans. This means that marine stratiform clouds are highly sensitive to changes by an addition of aerosols to act as CCN. This is the mechanism by which ship tracks appear very bright in

satellite imagery (Hobbs, 1993). Aerosols from ships and their effect on clouds and atmospheric cooling will be described in greater detail later in the chapter, with more specific model details discussed in Chapter 3.

Other Aerosol Radiative Effects

Aerosols also affect the lifetime of clouds. A cloud with a greater number density of CCN has smaller cloud droplets than a cloud with few CCN because these CCN must 'compete' with one another for water. These smaller droplets have lower collision efficiency, which suppresses precipitation and extends the lifetime of the cloud (Berner and Berner, 2012). Radiative effects due to the second indirect effect are still highly uncertain (Chandrakar et al., 2018). An aerosol "semi-direct" effect is also caused by black carbon aerosols, which have a very low SSA and warm the warm the surrounding air. This shortens the lifetime of clouds through "burn-off" and thus reduces albedo, causing warming (Box and Box, 2016). The total radiative forcing of the aerosol direct and indirect effects is estimated to be -0.9 to $-1.4\mathrm{Wm}^{-2}$, though this range has considerable uncertainty (Cherian et al., 2017). Overall, aerosols have a cooling effect on the Earth's atmosphere. We do not consider these other aerosol effects in our study.

2.1.3 Sulfur Dioxide and Sulfate Aerosols

Sulfur dioxide (SO_2) is a colourless, toxic gas produced by fossil fuel combustion and volcanic eruptions. It reacts with moisture in the upper respiratory system and may cause nerve damage in these areas, as well as respiratory infections, bronchitis, and cardiac disease. Exceeding WHO recommended 10-minute mean exposure limits cause measurable, short-term respiratory problems in people with asthma (World Health Organization, 2018)(Meng and Liu, 2007).

In the gas phase, sulfur dioxide reacts with OH to produce sulfuric acid, H_2SO_4:

$$SO_2 + OH + M \longrightarrow HSO_3 + M$$

$$HSO_3 + O_2 \longrightarrow SO_3 + HO_2$$

$$SO_3 + H_2O + M \longrightarrow H_2SO_4 + M$$

Alternatively, oxidation of SO_2 can take place in the aqueous phase in cloud and rain droplets:

$$SO_2(g) \longleftrightarrow SO_2 \cdot H_2O$$

$$SO_2 \cdot H_2O \longleftrightarrow {HSO_3}^- + H^+$$

$$H_2O_2(g) \longleftrightarrow H_2O_2(aq)$$

$${HSO_3}^- + H_2O_2(aq) + H^+ \longrightarrow {SO_4}^{2-} + 2\,H^+ + H_2O$$

This process occurs much faster than the gas phase oxidation (Jacob, 1999). Both processes lead to sulfate (${SO_4}^{2-}$) aerosols through condensation on other particles in the atmosphere. Atmospheric sulfuric acid also leads to acid rain due to its high stability. This high solubility, along with their average size, allows atmosphere sulfuric acid aerosols to make good CCN (Berner and Berner, 2012). 65% of sulfate aerosols are from anthropogenic sources: 63% from fossil fuel burning and 2% from biomass burning. Natural sources include dimethyl sulfate produced by bacteria and volcanic sulfur (Berner and Berner, 2012).

Sulfate aerosols have high a SSA. The direct effect of sulfur aerosols is estimated to have an overall global radiative forcing of -0.4±0.2Wm^{-2}, leading to cooling of the Earth's surface and atmosphere of approximately 0.8°C (Berner and Berner, 2012)(Brasseur et al., 1999). Sulfate aerosols dominate anthropogenic aerosol radiative forcing, with particularly high concentrations in Southeast Asia, and the Indian and Pacific Oceans.

It is difficult quantify the effects of the first indirect effect caused by anthropogenic sulfate aerosols. However, a 2005 study estimated that removing all sulfate aerosols would increase global precipitation by 3% (Brasseur and Roeckner, 2005) due to the first indirect effect.

2.1.4 Black Carbon

Black carbon (BC) is a primary aerosol created during incomplete combustion. It is mainly formed when burning fossil fuel or biomass (Berner and Berner, 2012). The exact definition of BC is often unclear, leading to inconsistencies between studies. BC is generally identified by its absorption of light, in contrast to elemental carbon (EC), which is usually measured using thermal-optical methods. However, there is no standard method to measuring BC or EC (Stiller et al., 2012), likely due in part to a lack of clear definitions. The Institute of Marine Engineering, Science and Technology proposed the following description of black carbon to be used by the International Maritime Organization:

> Black Carbon (BC) is strongly light absorbing carbonaceous material emitted as solid particulate matter created through incomplete combustion of carbon-based fuels. BC contains more than 80% carbon by mass, a high fraction of which is sp2-bonded carbon, and when emitted forms aggregates of primary spherules between 20 and 50 nm in aerodynamic diameter. BC absorbs solar radiation across all visible wavelengths and freshly emitted BC has a mass absorption efficiency of 5 $m^2 g^{-1}$ at the mid-visible wavelength of 550 nm. The strength of this light absorption varies with the composition, shape, size distribution, and mixing state of the particle.

Like many aerosols, black carbon causes health problems. However, because of its tenuous definition, it is difficult to compare studies that have examined this impact. European epidemiological studies have often used light absorbance of $PM_{2.5}$ filters as a way of inferring population exposure to BC particles, whereas North American studies were more likely to use EC content of these filters (Stiller et al., 2012). Nevertheless, a systematic review of many BC studies has provided evidence of short-term and long-term cardiopulmonary problems related to BC exposure.

BC has a large impact on climate and is the second-largest cause of human-induced climate change, despite only remaining in the atmosphere for about one week (Comer et al., 2017)(Bond et al., 2004). BC absorbs both direct solar radiation and solar

radiation that was scattered by clouds and other aerosols. This absorbed radiation therefore does not reach the Earth's surface, causing warming in the lower atmosphere where the BC is present (2.6 Wm^{-2}), and cooling at the surface where radiation is reduced (-1.7 Wm^{-2}). These direct effects lead to an overall warming of 0.9 Wm^{-2} at the top of the atmosphere (Berner and Berner, 2012). Great uncertainty arises in many of the estimates of the BC direct radiative effect due to model oversimplifications in the population and morphological mixing states of BC aerosols and an underestimation of concentration (Soares et al., 2018). Population mixing state is the degree of which BC is mixed with other aerosol species, ranging from entirely separate from other species (externally mixed) or mixed to some degree (internally mixed) (Kodros et al., 2018). Morphological mixing state refers to the chemical composition of aerosols and how it is distributed over and within its surface. Models generally assume aerosol populations to be completely externally or internally mixed rather than a more intermediate state more commonly observed in the atmosphere (Kodros et al., 2018)(Lesins et al., 2002). When complete internal mixing is assumed, the aerosols tend to be more absorbing than external mixtures. Internal mixtures of varying degrees are usually simulated through two methods: particles that are homogeneously mixed together and coated aerosols. The latter may often be achieved through a simple weighting factor (Box and Box, 2016).

BC can also act as CCN, leading to bright clouds and reduced precipitation through the first indirect effect, causing radiative forcing of $0.13 \pm 0.1 Wm^{-2}$. However, this first indirect effect of BC is highly uncertain due to its high absorption (Cherian et al., 2017). For example, BC may also increase warming in atmospheric brown clouds of 0.25°C/decade (Ramana et al., 2010). Atmospheric brown clouds may be transported long distances and cause warming over large areas.

Deposition of BC will also lead to warming, especially over high-albedo surfaces such as snow where sunlight is normally scattered. This effect is intensified during

the spring when solar radiation is more strongly absorbed over longer periods of time (Ramana et al., 2010).

2.1.5 Organic Carbon

The radiative effects of BC from a given emission source is affected by the relative concentrations of emitted organic carbon (OC) from that source. Organic carbon aerosols are created through both primary and secondary mechanisms: they are formed through condensation of volatile organic compounds (VOCs) that are emitted directly, as well as secondary products formed by photochemical reactions with these VOCs. Unlike BC, OC tends to scatter light, contributing to an atmospheric cooling effect like most other aerosols. Organic carbon is not the same as organic matter (OM), which includes compounds with hydrogen and oxygen bonded to the carbon atoms (Bond et al., 2004).

The ratio of BC to OC emissions from a particular source depends on many factors. This leads to uncertainty in predicted radiative effects. There are, however, general trends: fossil fuel combustion tends to produce much more BC than OC. Biomass burning, on the other hand, tends to produce much more OC.

OC from fossil fuel combustion leads to a direct effect of -0.09 $\pm$ 0.07 Wm^{-2} (Pachauri and Meyer, 2014).

2.2 Ship Emissions

The main atmospheric pollutants emitted from ships include sulfur oxides, nitrogen oxides, PM_{10}, $PM_{2.5}$, carbon monoxide, and black and organic carbon. Pollution from ships is caused by several factors, including the fuel used, the engine, and the engine efficiency (Pham and Nguyen, 2017). Different compounds emitted are affected by different ship properties. For example, sulfur dioxide emissions depend mainly on the sulfur content in the fuel used, whereas black carbon emissions depend on all three

of these factors. As such, regulating each of these emissions often requires different approaches. Ship emissions cause many human health problems, particularly in coastal areas (Johansson et al., 2017), with the effects increasing over the past several decades (Walker et al., 2018). Under the current emission trends, shipping is responsible for approximately 14 million childhood asthma cases each year (Sofiev et al., 2018). These trends are also estimated to be responsible for 3.6% of air pollution-related deaths from WHO and World Bank estimates, and 7% of cardiovascular- and cardiopulmonary-related mortality. Shipping, like other sources of aerosols, also contributes to the global direct and indirect effects and leads to changes in global temperatures. The following section will examine previous studies designed to quantify past and future climate effects due to shipping emissions. Future projections are based around zero compliance with sulfur regulations ("business as usual") or full compliance.

2.2.1 Sulfur Emissions and Restrictions

The radiative effects of current and future ship emissions have been the focus of several recent studies. Earlier studies found that sulfate emissions from ships lead to a global atmospheric cooling between -47 mWm^{-2} to -8 mWm^{-2} for the direct effect and -600 mWm^{-2} to -38 mWm^{-2} for the indirect effect (Lund et al. 2012; Lauer et al. 2009; Balkanski et al. 2010; Corbett et al. 2010; Fuglestvedt et al. 2008). A more recent study found lower cooling effect projections for 2020 (BAU): -6.7 mWm^{-2} from the direct effect and -86 mWm^{-2} from the first indirect effect, leading to an overall cooling of -93 mWm^{-2} from sulfate aerosols emitted from ships (Sofiev et al., 2018). These estimates consider the projected growth of the shipping industry that will lead to more ship travel and an increase in fuel demand worldwide.

Sofiev et al. also predicted the reduction in cooling due to the IMO regulations. They calculated a 3.8 mWm^{-2} reduction in cooling from the direct effect and a 67

mWm^{-2} reduction in cooling from the first indirect effect. This leads to an overall reduction in cooling of 71 mWm^{-2} (Sofiev et al., 2018). Calculations of the first indirect effect have a lot of uncertainty, however: predicting the degree of mixing of sulfate aerosols within clouds is difficult and depends on the individual clouds themselves.

2.2.2 Black Carbon Emissions

Along with sulfate aerosols, ships also emit a lot of black carbon. This is largely attributed to high use of diesel engines in the shipping industry. Between 0.7 – 2% of present-day global BC emissions are from international commercial shipping (International Maritime Organization 2015; Comer et al. 2017; Klimont et al. 2017). Whereas sulfate emissions are directly proportional to the sulfur content of the unburned fuel, BC emissions depend on more factors than the chemical constituents of the fuel. This makes BC emissions much more difficult to regulate. Engine load, fuel quality, the presence of scrubber technology (an exhaust cleaning system), and ship stroke type all affect BC ship emissions (Lack and Corbett, 2012)(Comer et al., 2017). Ships operating with a lower engine load, often due to variable ship speed, tend to combust the fuel less efficiently, leading to higher production of carbon monoxide and BC unless adjustments to the engine are made (International Maritime Organization, 2015). Fuel with high levels of impurities such as sulfur, heavy metals, and heavy hydrocarbons will also produce more BC. Ship scrubbers installed on ships to remove sulfate aerosols may also reduce BC, though this has not been extensively studied (Lack and Corbett, 2012). According to a 2015 report by the International Council on Clean Transportation, "Accounting for BC's global warming potential, ship BC emissions were responsible for 5% to 8% (100-year timescale) and 16% to 23% (20-year timescale) of the CO_2-equivalent climate warming impact from shipping in 2015" (Comer et al., 2017). It is therefore important to implement restrictions on BC from

ships, a challenge that the IMO has begun to investigate (International Maritime Organization, 2015).

Several studies have examined the direct radiative effect of BC from global shipping. A 2010 study estimated that when internal mixing is assumed, shipping BC had a positive radiative effect of 1.1 ± 0.5 mWm^{-2}. For external mixing, shipping BC had a radiative effect of 1.6 ± 0.5 mWm^{-2} (Balkanski et al., 2010). These results were noted to be in agreement with earlier work using different models (Fuglestvedt et al., 2008).

2.2.3 Organic Carbon Emissions

Widespread use of diesel engines in the shipping industry leads to a high ratio of BC to OC compared to other sources such as biomass burning. However, considering both of these emissions together leads to a more complete understanding of shipping radiative effects (Fuglestvedt et al., 2008). Implementing BC restrictions on the shipping industry will likely lead to reduced OC emissions, reducing the cooling effect of BC restrictions. Therefore, OC emissions must be considered alongside BC emissions.

2.2.4 Relationships Between Black Carbon, Organic Carbon, and Sulfate

The atmospheric warming due to black carbon in a plume is dependent on the presence of sulfate and other high albedo aerosols such as OC. A high BC-to-sulfate ratio leads to more efficient solar absorption. Historically, this ratio in shipping emissions has been comparatively lower than other sources due to usage of low-quality fuel containing high sulfur concentrations (Ramana et al., 2010). The presence of OC in shipping plumes further offsets the warming due to BC. The relative concentrations of SO_4^{2-}, BC, and OC must therefore all be considered to determine the overall radiative

effects from shipping emissions.

This thesis focuses on the effects of a global 85% reduction of SO_2 from ships, an approximation of the global IMO sulfur restrictions scheduled for 2020. The location and magnitude of reduced aerosols are examined, and the direct and indirect radiative effects of this reduction are calculated. We then examine the effects of an equal reduction in BC and OC aerosols from ships and perform identical calculations. These reductions are compared: would the implementation of identical global restrictions on BC emissions offset the warming caused by the sulfur restrictions? Does this change when OC emissions are also restricted?

Finally, we consider the reduction of CO_2 necessary to make each of these scenarios climate-neutral.

The following chapter describes the chemical transport model and the additional modules used to perform the calculations in this project. Chapter 4 presents and interprets the results of the project. The thesis is concluded in chapter 5, where future work is outlined.

Chapter 3

Model and Methods

Chemical transport models (CTMs) are mathematical models that describe the changing atmospheric concentrations through space and time across the globe. There are two main types of CTMs: Eulerian (used in this project) and Lagrangian. Eulerian CTMs employ a simple "box model" that divide the Earth up into numerous boxes, often of equal size. Within each box, the concentrations of atmospheric substances are affected by simulated processes such as transport, chemistry, emissions, and deposition. The CTM receives meteorological data as input and solves the continuity equation to determine atmospheric concentrations (Jacob, 1999). A continuity equation describes the transport of a material. In atmospheric chemistry, there are many chemicals of interest with transport that must be described with this equation. In the Eulerian model, the continuity equation describes transport in and out of a given box.

3.1 The Continuity Equation

Consider the number density, $n(X,t)$, of a chemical species in a three-dimensional box fixed to the earth. X is a spatial Cartesian coordinates vector. The box has a volume $dV{=}dxdydz$. The number density of this species changes through time as it may be subject to transport to another box, increased through sources and chemical reactions (production, P), and decreased through sinks and other chemical reactions

(loss, L). We describe the transport to another box (the flux, F, in molecules per cm^2 per second) in the x direction across the plane $dA = dydz$ by the amount dx through the following equation:

$$\frac{F_x(x)dydz - F_x(x+dx)dydz}{dxdydz} = F_x(x)dx - F_x(x+dx)dx = \frac{\partial F_x}{\partial x} \tag{3.1}$$

In the y and z directions, the transport is $\partial Fy/\partial y$ and $\partial Fz/\partial z$. The change in the number density of the species may be written as the sum of the transport, source, and sink terms:

$$\frac{\partial n_x}{\partial t} = -\frac{\partial F_x}{\partial x} - \frac{\partial F_y}{\partial y} - \frac{\partial F_z}{\partial z} + P - L = -\nabla \cdot F + P \breve{} L \tag{3.2}$$

where $\nabla \cdot F$ is the flux divergence. This is the continuity equation the CTMs solve. This cannot be done analytically; computer simulations are used to perform the calculation numerically (Jacob, 1999).

3.2 GEOS-Chem

One of the many available chemical transport models used to solve the continuity equation is GEOS-Chem (Bey et al., 2001). GEOS-Chem is a 3-dimensional CTM that uses meteorological input from the Goddard Earth Observing System (GEOS) from the NASA Global Modeling and Assimilation Office (GMAO). The current operational meteorological data product is GEOS-Chem Forward-Processing (GEOS-FP). Meteorological inputs from GMAO include wind direction and speed, temperatures, moisture, cloud distributions and in-cloud transport (Pawson, 2017). Liquid water content (LWC) is calculated from these inputs. This meteorological data is either instantaneous or time-averaged. Instantaneous collections of data contain meteorological information written every 3 hours. Time-averaged data, on the other hand, is a continuous collection of data that is time-averaged every hour (for 2-D fields) or

every 3 hours (for 3-D fields).

The horizontal grid resolution of GEOS-FP data is 0.25°×0.3125°. This is re-gridded onto a 2°×2.5° grid for use with the standard GEOS-Chem model. The vertical grid includes 47 pressure layers from the surface of the Earth to the top of the atmosphere at 0.01 hPa. The pressure and height difference in each layer vary with altitude, with the bottom layer extending 59m and 7.6 hPa. The vertical cloud coherence is determined using approximate random overlap, an assumption that clouds in each vertical layer are independently determined.

3.2.1 Model Chemistry

GEOS-Chem allows users to select from a number of chemistry mechanisms. For this project, the tropospheric chemistry mechanism (known as "tropchem" or the "NO_x-O_x-hydrocarbon-aerosol-Br-Cl-I" mechanism) was used. This mechanism provides the full GEOS-Chem chemistry mechanisms, including kinetic and photolysis reactions, but excludes the stratosphere (Eastham et al., 2014) The default simple secondary organic aerosol (SOA) scheme was used. This scheme provides a direct relationship between emissions and SOA yields.

3.2.2 HEMCO and Emission Inventories

GEOS-Chem, like other CTMs, requires information on atmospheric species in order to produce meaningful results. This includes information on emissions. The current version of GEOS-Chem uses Harvard-NASA Emissions Component (HEMCO) to compute global emissions. HEMCO is a stand-alone software component that allows users to include emission inventories in their simulations. Emission inventories may be bottom-up, which estimates emission based on activity rates such as fuel burning, or top-down, meaning the emissions are estimated using atmospheric observations (Keller et al., 2014). HEMCO acts as a link between emissions data and

the simulations that use them and allows for changes to the inventories to be easily made. For example, scale factors can be added using the HEMCO user interface to increase or reduce the concentrations of the emitted species. This is useful when performing sensitivity simulations. Many scale factors are included in HEMCO to account for variation in emissions due to season, time of day, year, etc. Emission inventories used by HEMCO may have any spatial or temporal resolutions, leading to easy implementation of new inventories. Table 3.1 shows the emission inventories used in each simulation. The following inventories contain ship emissions that were scaled during the sensitivity studies: The ARCTAS SO_2 emissions inventory is based on the work by Eyring et. al in a 2005 study that estimated total international shipping emissions for 1985, 1990, 2000, and created projections for 2020 (Eyring et al., 2005). The values of emissions for any given year are calculated by HEMCO from the estimations of the specified years from the study. The spatial pattern of the SO_2 emissions is based on the emissions patterns from the year 2000. The Community Emissions Data System (CEDS) contains the hydrophobic and hydrophilic black and organic carbon emissions from ships. It is a global emissions inventory available for the years 1950 to 2014 (Hoesly et al., 2018). Shipping emissions in this inventory include (SO_2, NO_x, CO, NMVOCs, NH_3, BC, OC, CO_2, and CH_4)

Inventory	Species of interest	Resolution	Reference
ARCTAS	SO_2	$1°\times1°$	Eyring et al., 2005
CEDS	BC, OC	$0.5°\times0.5°$	Hoesly et al., 2018

Table 3.1: HEMCO species of interest used

3.2.3 TOMAS

Calculating the direct and indirect radiative effects of shipping emission restrictions requires the use of a software package not present in the GEOS-Chem base model. The TwO-Moment Aerosol Sectional (TOMAS) tracks the number and mass (two

independent moments) of aerosols, including sulfate and hydrophobic and hydrophilic black carbon, in GEOS-Chem simulations. TOMAS keeps track of aerosol size using discrete size bins (15 in this project). Thirteen bins are logarithmically spaced from 3nm to 1μm, and two bins keep track of aerosols from 1 – 10 μm. The two moments, aerosol number (N_k) and aerosol mass (M_k) in the k-th size bin are defined as

$$N_k = \int_{x_k}^{x_k+1} n_k(x)dx \tag{3.3}$$

and

$$M_k = \int_{x_k}^{x_k+1} xn_k(x)dx \tag{3.4}$$

where x_k and x_{k+1} are the size limits of the k-th bin. The ratio between N_k and M_k may vary through space and time and are independent of one another. Considering these two moments allows for more accurate prediction and conservation of aerosol number than models using single-moment calculations (Adams and Seinfeld, 2002).

Particles simulated by TOMAS are emitted directly or formed using a new particle formation scheme. Sulfate aerosols are formed using a $H_2SO_4-NH_3-H_2O$ nucleation scheme. This scheme uses a lookup-table of simulated formation rates as a function of sulfuric acid and ammonia vapor concentrations, relative humidity, and temperature (Baranizadeh et al., 2016). Black carbon aerosols are emitted directly. In TOMAS, particles grow through coagulation and condensation. TOMAS uses the Brownian coagulation scheme of Fuchs to consider coagulation between particles of all sizes (Fuchs et al., 1965). During coagulation, particles fuse together, gaining mass and reducing the overall number of aerosols. Condensation allows the particles to grow, but this does not reduce their numbers (Croft et al., 2016).

Particles are removed from the atmosphere through precipitation in and below clouds, dry deposition (using the resistance-in-series approach of Wesley (1989)), and in-cloud scavenging.

In the TOMAS simiulations used for this project, external mixing of BC and OC aerosols is assumed. In addition, the hydrophilic BC absorption factor is multiplied by a constant factor of 1.5 to simulate enhanced absorption within an external mixture and assume an "approximate midpoint" between external mixing and internal mixing of BC aerosols (Kodros et al., 2018). This assumption was recommended in a 2006 investigative review (Bond and Bergstrom, 2006) Internal mixing is implemented in post-processing scripts for the relevant scenarios (Kodros et al., 2018).

3.2.4 RRTMG

Calculating the radiative effects of shipping emission restrictions also requires the Rapid Radiative Transfer Model for General Circulation Models (RRTMG). RRTMG allows users to calculate longwave and shortwave radiative fluxes at various levels in the Earth's atmosphere. To calculate this information, the RRTMG code "utilizes the correlated-k approach to calculate fluxes and heating rates efficiently and accurately" (Iacono et al., 2008). The k distributions are taken from the radiative transfer code LBLRTM (line-by-line radiative transfer model), developed in the 1990s (Clough et al., 2005). The Monte Carlo Independent Column Approximation is also implemented in RRTMG calculations. The use of TOMAS and RRTMG to calculate the radiative effects follows the methods used in Kodros et al. 2018.

Direct Radiative Effect Calculations

The direct radiative effects caused by the reduction in shipping emissions is calculated using both TOMAS and RRTMG. Aerosol optical properties are calculated using monthly-averaged aerosol mass and number concentrations determined by TOMAS and refractive indices using the Global Aerosol Dataset (GADS) (Koepke et al., 1997). Mie code is also used to determine aerosol optical depth, single scattering albedo, and asymmetry parameters through approximations that assume aerosols are spherical

and homogeneously coated or uncoated (Bohren and Huffman, 1983). These values, along with surface albedo and the cloud fractions from GEOS-FP meteorology, are input into offline RRTMG code to calculate the change in solar flux at the top of the atmosphere(Croft et al., 2019).

Figure 3.1: DRE calculations

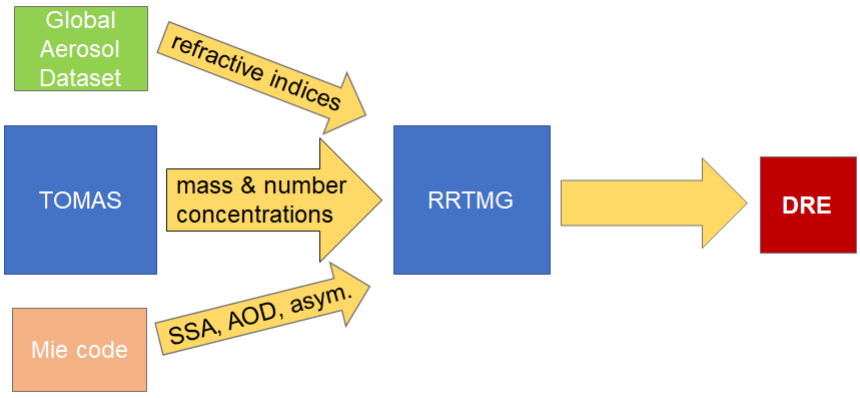

Indirect Radiative Effect Calculations

Calculations of the first aerosol indirect effect also use particle mass and number concentrations determined by TOMAS. In addition, parameterization of aerosol activation (formation of a cloud droplet) from a 2002 study is used (Abdul-Razzak and Ghan, 2002). This parameterization calculates the critical supersaturation for particles of arbitrary size. This information is used to calculate cloud droplet number concentrations (CDNC). In order to determine the change in the solar flux at the top of the atmosphere due to changes in CCN radius, an effective cloud drop radius of r_1 = 10μm is assumed as a control. This value is then perturbed by calculating

$$r_2 = r_1 \times \left(\frac{\mathrm{CDNC}_1}{\mathrm{CDNC}_2}\right)^{\frac{1}{3}} \tag{3.5}$$

where CDNC_2 is the CDNC calculated for the case of OC or SO_2 perturbations (Scott et al., 2014). This information is then used in offline RRTMG code to calculate the

change in solar flux at the top of the atmosphere (Kodros et al., 2016).

Figure 3.2: AIE calculations

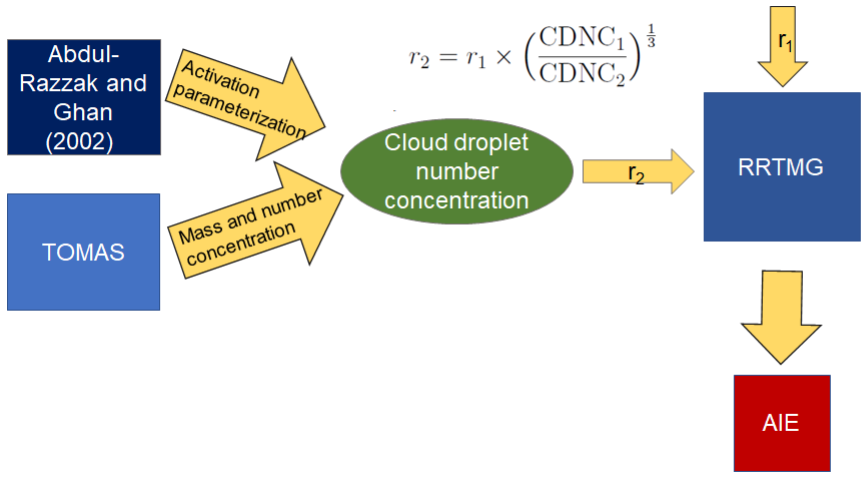

3.2.5 GEOS-Chem runs conducted

GEOS-Chem version 12.0.3 was used to calculate changes to

- atmospheric concentrations of SO_2, SO_4^{2-}, hydrophilic OC and BC, hydrophobic OC and BC
- direct radiative effect
- aerosol indirect effect

due to scenarios involving an 85% reductions in SO_2, BC, and OC emissions. The simulations were conducted for one year from January 2013 to January 2014 using GEOS-FP meteorological data for that period. The model resolution was $4°\times5°$. For all simulations, transport and convection calculations were performed every 15 minutes, and chemistry and emission calculations were performed every 30 minutes.

Chapter 4

Results and Discussion

4.1 Sulfur dioxide

Table 4.1 outlines the different scenarios simulated in this project. Figure 4.1a shows all SO_2 emitted from ships in the in the 'BAU' scenario. The greatest concentrations can be found near coastlines with high ship traffic, which is consistent with global shipping tracks shown previous studies (Walker et al. 2018; Johansson et al. 2017; Lauer et al. 2009). The greatest concentration of SO_2 in these areas is approximately 0.7 $\mu g/m^3$. The global mean concentration is 0.0468 $\mu g/m^3$.

Figure 4.1b shows all SO_4^{2-} from ships in the 'BAU' scenario. The patterns are similar to those from Figure 4.1a, but the tracks cover a broader geographic area. In areas of high ship traffic, the concentrations of SO_4^{2-} formed from shipping emissions is lower than SO_2. SO_4^{2-} is formed when SO_2 reacts with other species, as outlined in Section 2.1.3. The global mean concentration is 0.0687 $\mu g/m^3$.

Figure 4.2 shows the direct and indirect radiative effects of all shipping emissions. The global mean DRE is -33 mWm^{-2} and is shown in Figure 4.2a. The areas of greatest cooling include the northeast and northwest Pacific Ocean, the North Sea, and the Indian Ocean. The global mean AIE is shown in Figure 4.2 and shows the

Table 4.1: Simulations run

'BAU' scenario	**'IMO' scenario**	**'BC restriction' scenario**	**'BC & OC restriction' scenario**
shipping emissions are turned on & unchanged	SO_2 emissions from ships are reduced by 85%	BC emissions from ships are reduced by 85%	BC and OC emissions from ships are reduced by 85%

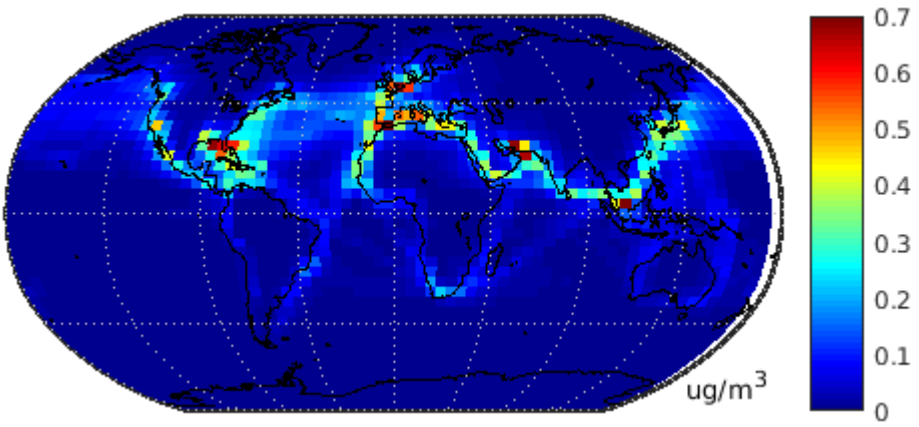

(a) SO_2 emissions in the 'BAU' scenario.

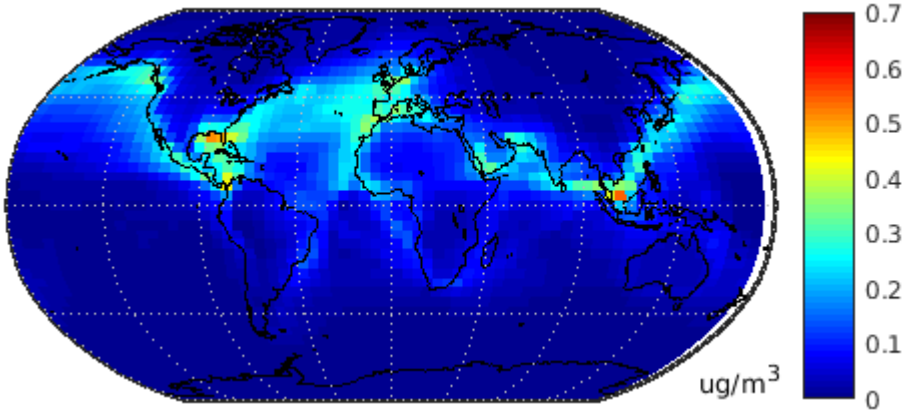

(b) SO_4^{2-} emissions in the 'BAU' scenario.

Figure 4.1: SO_2 and SO_4^{2-} concentrations in the BAU scenario

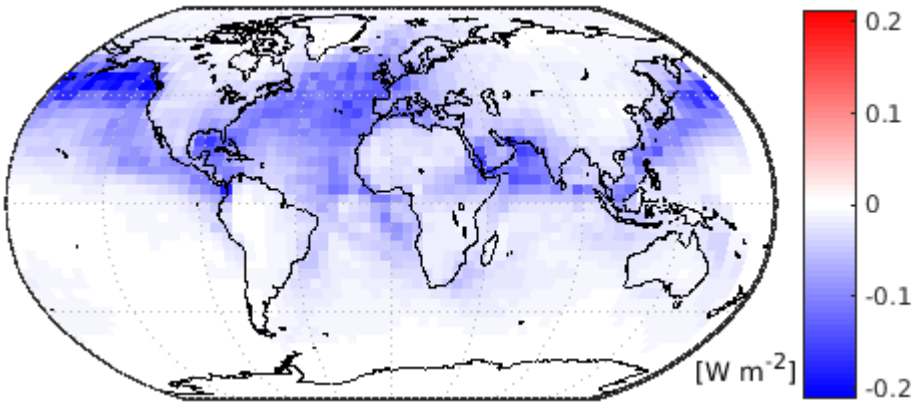

(a) DRE due to the 'BAU' scenario. The global mean is -33.3 mWm^{-2}

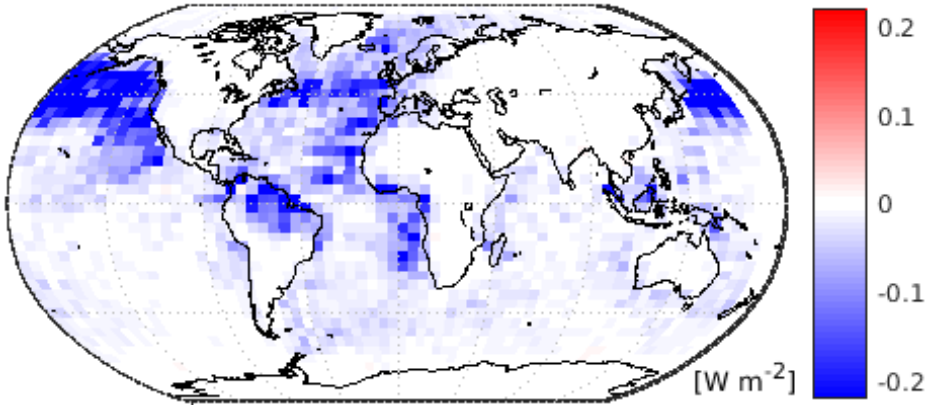

(b) AIE due to the ''BAU' scenario. The global mean is -31.1 mWm^{-2}.

Figure 4.2: Radiative effects of 'BAU' scenario. The total radiative effects from shipping emissions in this scenario is -64.4 mWm^{-2}

greatest cooling in similar regions, with the addition of the Atlantic Ocean region north of Brazil, and no cooling over the Indian Ocean. Overall, the total radiative effects from all shipping emissions leads to -64.4 mWm^{-2} of cooling.

Previous studies have estimated radiative effects of shipping emissions under the BAU scenario to be -47 to -7 mWm^{-2} for the DRE and -600 to -38 mWm^{-2} for the AIE (Sofiev et al. 2018; Lund et al. 2012; Fuglestvedt et al. 2008; Balkanski et al. 2010; Corbett et al. 2010; Lauer et al. 2009). Our calculation of the DRE falls within this range. However, our calculation for the AIE is smaller in magnitude than estimated in previous studies. These studies also predict future shipping activities in different ways, and this can lead to differences in DRE and AIE calculatoins.

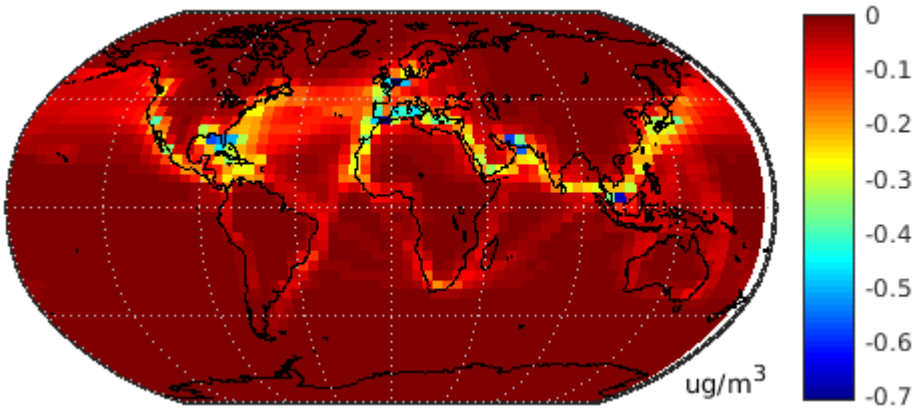

(a) Change in SO_2 concentrations due to the IMO scenario. The global mean reduction in concentration is 0.0398 $\mu g/m^3$.

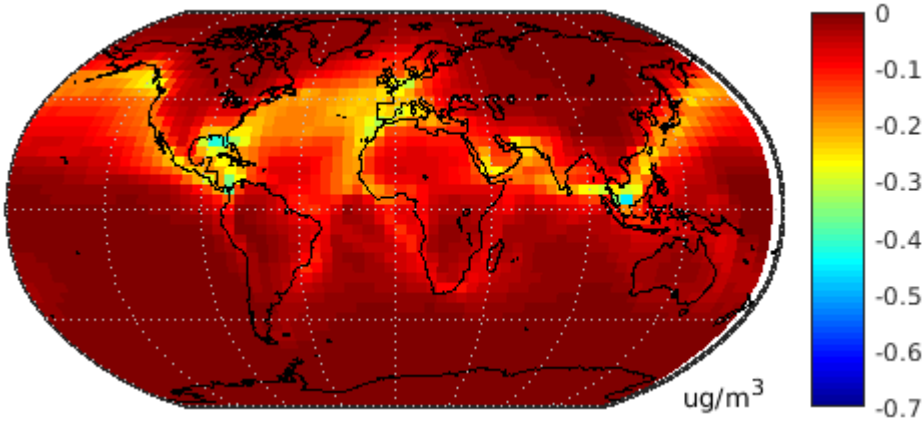

(b) Change in SO_4^{2-} concentrations due to the IMO scenario. The global mean reduction in concentration is 0.0584 $\mu g/m^3$

Figure 4.3: Change in SO_2 and SO_4^{2-} concentrations in the IMO scenario

Figure 4.3a shows the change in SO_2 concentrations in the IMO scenario. The greatest change in concentration occurs along ship tracks with the most traffic. The global mean reduction in concentration is 0.0398 $\mu g/m^3$. This results in a global mean concentration of SO_2 from ships of 0.0070 $\mu g/m^3$, a 90% reduction in shipping SO_2.

Figure 4.3b shows the change in SO_4^{2-} concentrations in the IMO scenario. The global mean concentration of SO_4^{2-} is reduced by 0.0584 $\mu g/m^3$, leading to a global mean concentration of 0.0103 $\mu g/m^3$. This is also 90% less than BAU levels.

The warming attributed to the IMO scenario is shown in Figure 4.4a. This is

the relative change compared to the 'BAU' scenario. The DRE occurs in the same geographic pattern as in Figure 4.3b, illustrating that the this effect occurs where SO_4^{2-} aerosols have been reduced and less scattering of sunlight occurs. Areas with significant changes are the northeastern Pacific Ocean, the Mediterranean Ocean, and the Indian Ocean. Some effect is observed over Europe and North Africa, but most of the change occurs over the ocean. The global mean change in DRE is 28.8 mWm^{-2}. Therefore, the global mean DRE from ships in the IMO scenario is -4.5 mWm^{-2}. Sofiev et al. 2018 estimated the IMO scenario would lead to a DRE from ships of -2.7 mWm^{-2}, a result similar in magnitude to ours.

The global mean change in AIE is shown in Figure 4.4b. The global mean warming caused by this change is 16.5 mWm^{-2}. Therefore, the AIE from shipping in the IMO has a global mean of -14.6 mWm^{-2}. Sofiev et al. 2018 predicted a global mean AIE from ships in this scenario to be -19 mWm^{-2}.

Overall, we calculated the global mean radiative effects to from the IMO scenario to be -19.1 mWm^{-2}. Sofiev et al. 2018 predicted the global mean radiative effects in this scenario to be -22 mWm^{-2}. Although their prediction of the BAU AIE was much larger than ours (a global average of 55 mWm^{-2} more cooling), our calculations of the IMO scenario AIE are much more similar. Partanen et al. 2013 predicted the AIE in this scenario to be between -40 to -60 mWm^{-2}.

In the studies that calculated AIE for various shipping scenarios, the global mean AIE estimates were much greater than the DRE estimates. In our results, however, this is not the case. It is difficult to determine the reason for this. One possibility may include differences in CCN radii and spatial distribution, but most studies do not present this information. The size and geographic location of CCN will affect their influence on cloud properties. Each study used different meterological fields with different reference years. The lack of consistency between studies may have resulted in different LWC values. However, LWC values are not reported by these

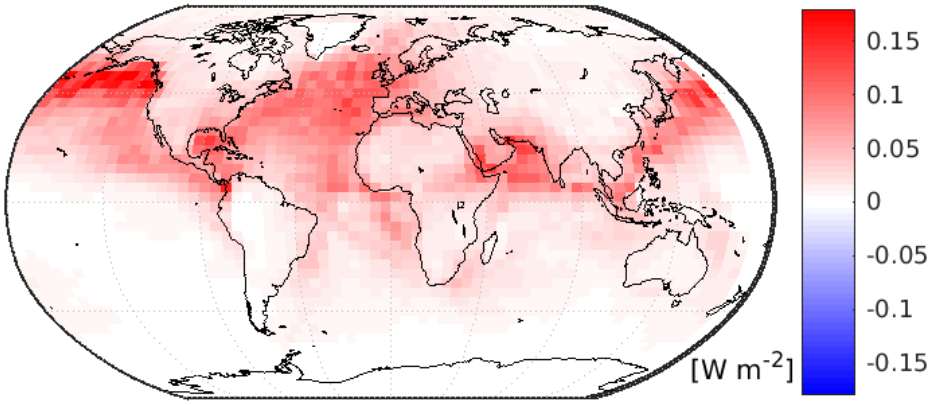

(a) Change in shipping DRE due to the IMO scenario. The global mean change is 28.8 mWm^{-2}. DRE from shipping in this scenario is -4.5 mWm^{-2}.

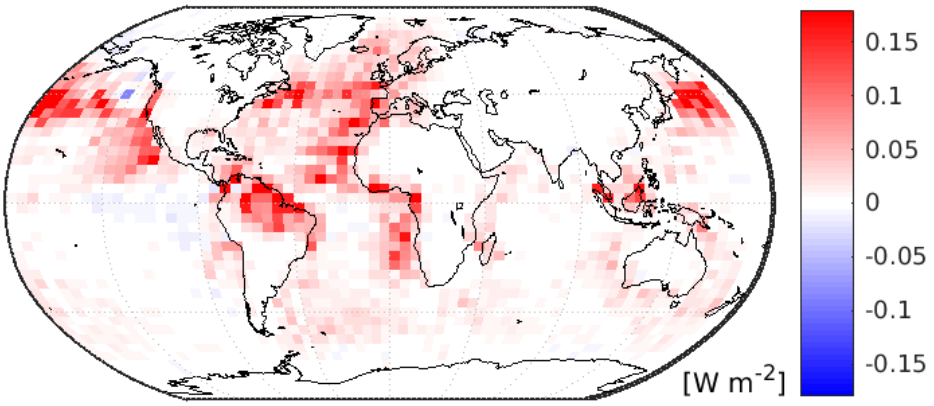

(b) Change in shipping AIE due to the IMO scenario. The global mean is change 16.5 mWm^{-2}. AIE from shipping in this scenario is -14.6 mWm^{-2}.

Figure 4.4: Radiative effects of shipping emissions in the IMO scenario. The global mean radiative effects of this scenario is -19.1 mWm^{-2}. This is a warming of 45.3 mWm^{-2} compared to BAU.

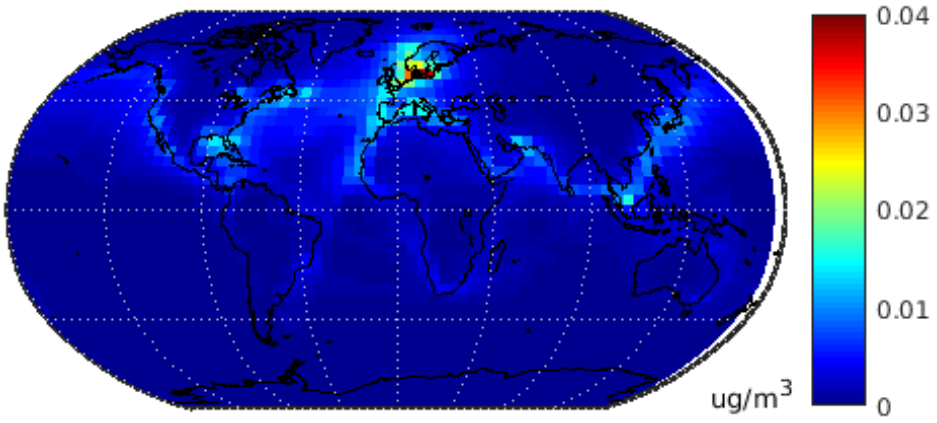

(a) BC concentrations in the 'BAU' scenario.

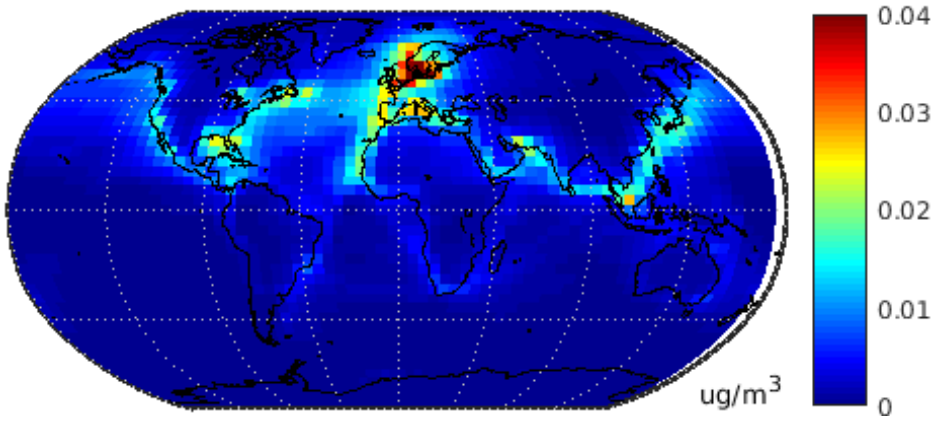

(b) BC and OC concentrations in the 'BAU' scenario.

Figure 4.5: BC and OC concentrations in the BAU scenario

studies. Another possibility may be related to the vertical cloud coherence in each model. In GEOS-Chem, this is determined using the approximate random overlap method, but with the execption of Balkanski et al. 2010, the other studies did not report how vertical cloud coherence was determined. AIE calculations still have a very high degree of uncertainty (Pachauri and Meyer, 2014).

4.2 Black and organic carbon

Figure 4.5a shows all BC emitted from ships in the 'BAU' scenario. The global mean concentration is 0.0020 $\mu g/m^3$. As with other ship-emitted species, the emissions follow the patterns of greatest shipping activity. The largest concentrations can be seen

in and around the North Sea, where shipping traffic is particularly high. Figure 4.5b shows all OC and BC emitted from ships in the 'BAU' scenario. The global mean concentration is 0.0034 $\mu g/m^3$. From this, we determine the global mean concentration of OC emissions from ships is 0.0014 $\mu g/m^3$.

Figure 4.6a shows the change in black carbon (hydrophilic and hydrophobic) concentrations due to the 'BC restriction' scenario. The global mean reduction of BC is 0.0017 $\mu g/m^3$, a reduction of 90%. The global atmospheric concentration of BC is 0.0003 $\mu g/m^3$. Figure 4.6b shows the change in black and organic carbon (hydrophilic and hydrophobic) due to the 'BC restriction' scenario. The global mean reduction of BC is 0.0029 $\mu g/m^3$, a reduction of 90%. The global atmospheric concentration of BC is 0.0008 $\mu g/m^3$.

Figure 4.7a shows the DRE due to the 'BC restriction' scenario where external mixing of the BC aerosols is assumed. The global mean DRE is -0.766 mWm^{-2}. The greatest DRE is found over the northern Indian Ocean, the North Sea, and northwestern Pacific Ocean, reaching values around 8 mWm^{-2}. When internal mixing is assumed, the global cooling due to the DRE is -1.3 mWm^{-2}, as shown in Figure 4.7b. Other studies have not examined the radiative effects of an 85% reduction in shipping BC, though Balkanski et al. 2010 found that the total concentration of BC from global shipping has a DRE of 1.3 - 22 mWm^{-2} when external mixing is assumed and 0.9 - 1 mWm^{-2} when internal mixing is assumed. These results have a similar magnitude.

Figure 4.8a shows the change in DRE due to the 'BC and OC restriction' scenario where external mixing of the BC aerosols is assumed. The global mean DRE is -0.581 mWm^{-2}. The cooling due to this scenario is smaller than the 'BC restriction' scenario by 0.185 mWm^{-2} because the reduction in OC has the opposite effect of a reduction in BC. However, even when OC is included, reducing these emissions together still leads to a cooling effect.

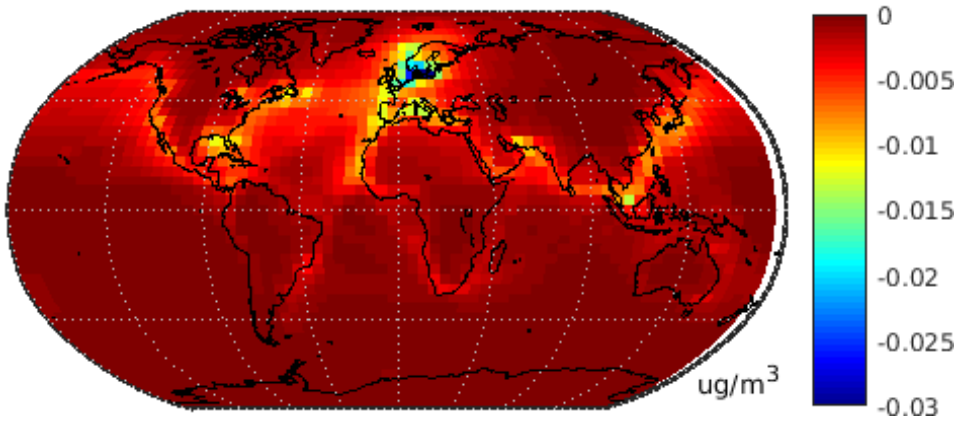

(a) Change in BC emissions in the 'BC restriction' scenario. The global mean reduction is 0.0017 $\mu g/m^3$.

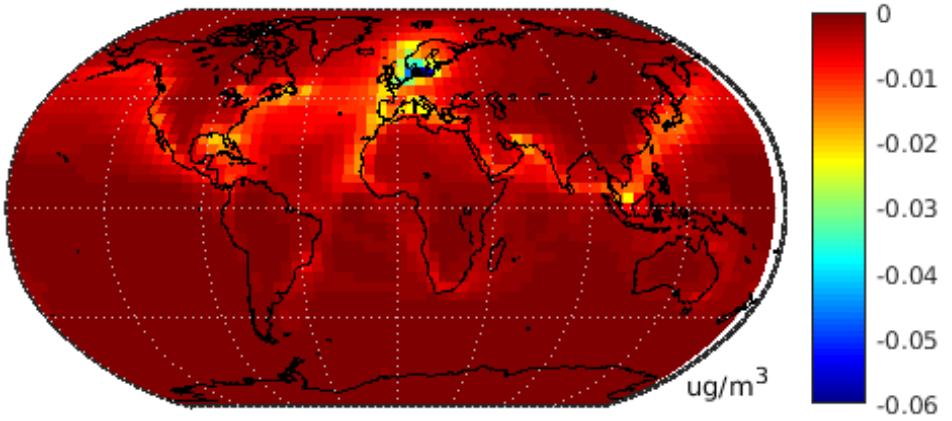

(b) Change in BC and OC emissions in the 'BC and OC restriction' scenario. The global mean reduction is 0.0029. $\mu g/m^3$.

Figure 4.6: Change in BC and OC concentrations in the 'BC restriction' and 'BC and OC restriction' scenarios

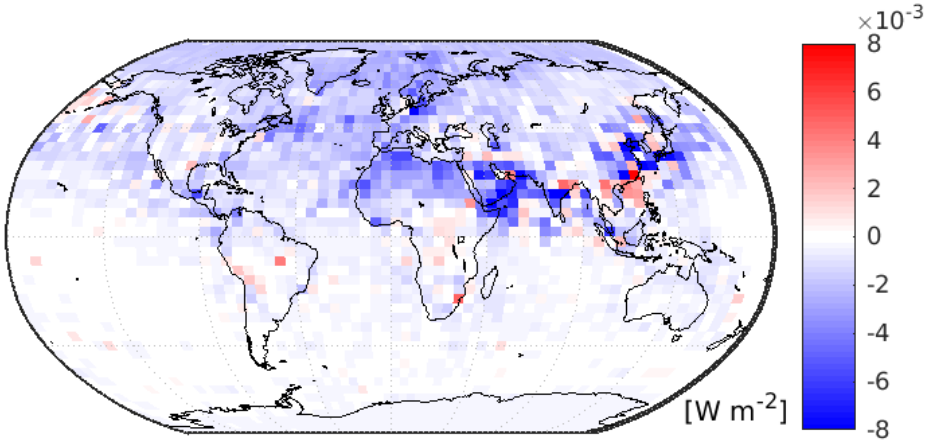

(a) Change in shipping DRE due to the 'BC restriction' scenario with external mixing assumed. The global mean is -0.766 mWm^{-2}

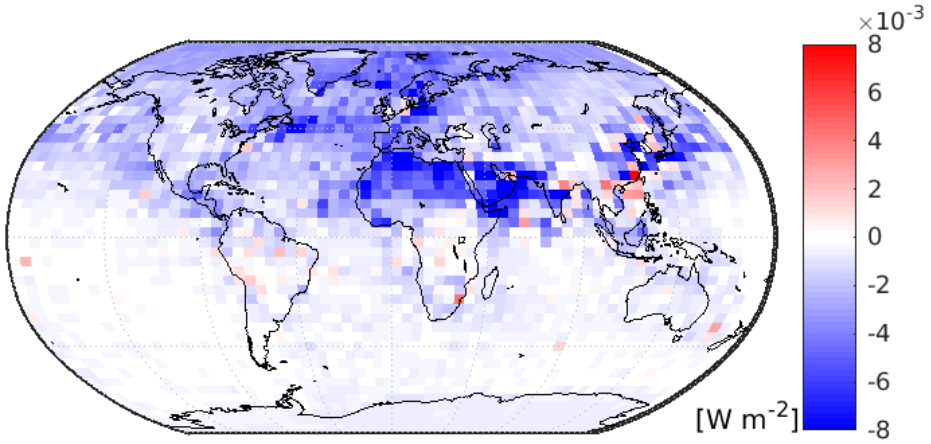

(b) Change in shipping DRE due to the 'BC restriction' scenario with internal mixing assumed. The global mean is -1.30 mWm^{-2}

Figure 4.7: Change in shipping DRE due to 'BC restriction' scenario for external and internal mixing

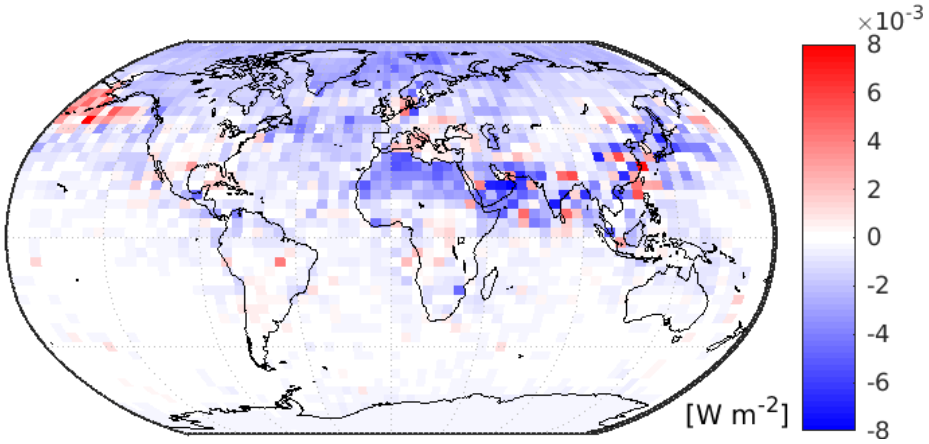

(a) Change in shipping DRE due to the 'BC and OC restriction' scenario with external mixing assumed. The global mean is -0.581 mWm^{-2}

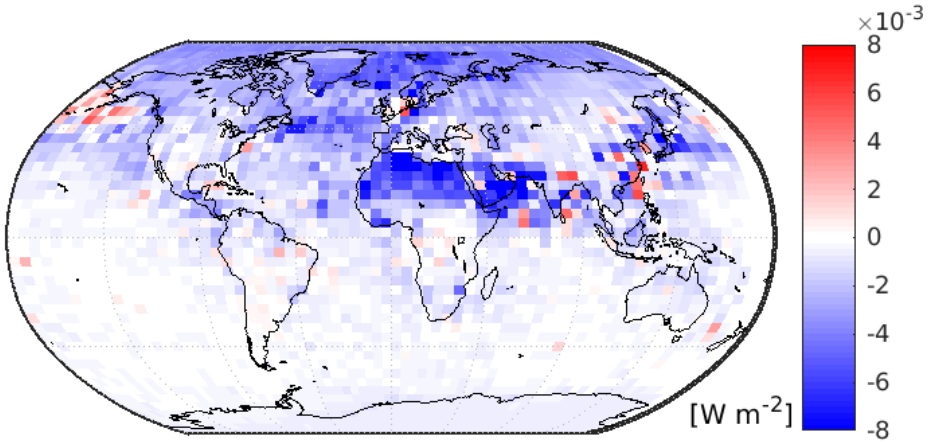

(b) Change in shipping DRE due to the 'BC and OC restriction' scenario with internal mixing assumed. The global mean is -1.10 mWm^{-2}

Figure 4.8: Change in shipping DRE due to 'BC restriction' scenario for external and internal mixing

Figure 4.8b shows the change in DRE due to the 'BC and OC restriction' scenario where internal mixing of the BC aerosols is assumed. The global mean cooling when OC and BC is reduced is -1.1 mWm^{-2}.

We summarize our results in Table 4.2. The BAU scenario has a total cooling of -64.4 mWm^{-2}. The net change of each other scenario are compared to this baseline. The IMO scenario has a total cooling of -19.1 mWm^{-2}. This is an overall warming of 45.3 mWm^{-2}.

An 85% BC emissions restriction alongside the IMO scenario reduces this overall

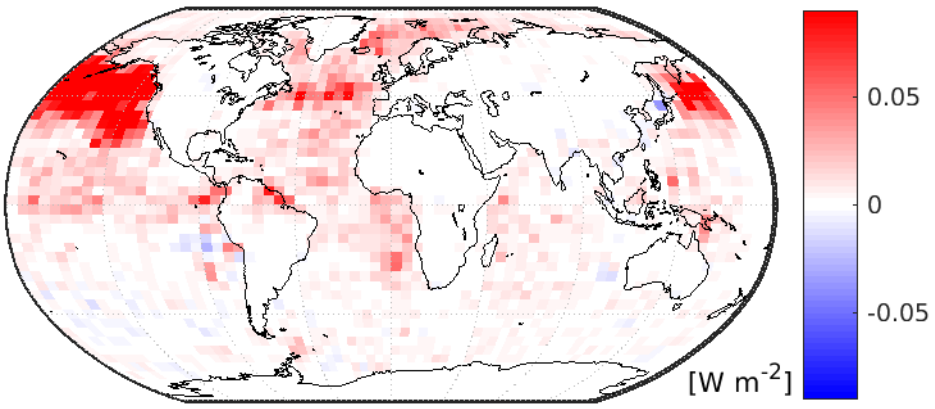

Figure 4.9: Change in shipping AIE due to the 'BC + OC restriction' scenario. The global mean is 9.60 mWm^{-2}

warming to 44 to 44.5 mWm^{-2}. This range is due to calculating the DRE assuming both external and internal mixing for BC. Assuming external mixing results in a cooling of -5.27 mWm^{-2}, and internal mixing results in -5.80 mWm^{-2} of cooling. A BC reduction does not lead to an AIE in our simulations.

The BC restriction scenario does not offset much of the warming caused by the IMO scenario. In the 'IMO + OC + BC' reduction scenario, OC is reduced by 85% alongside BC. This may be relevant for some emission control technologies. In this scenario, the overall warming is greater than in the IMO scenario. Any technological changes in the shipping industry designed to reduce BC emissions may lead to additional warming if OC is also reduced. It will be important for engineers and policymakers to consider the ratio of OC to BC when new technologies are considered. Otherwise, attempts designed to mitigate the warming caused by the IMO scenario may actually make it worse.

4.2.1 Carbon Dioxide

In order to make these scenarios climate-neutral, carbon dioxide reductions could be implemented. In 2013, ships collectively emitted 910 million tonnes of CO_2 (Olmer et al., 2017). According to a 2013 study by Joos et al., the Absolute Global Warming

Table 4.2: Summary of radiative effects of shipping emission scenarios. The scenario with the least warming relative to BAU is the IMO + BC restriction scenario.

Scenario	**DRE (mWm^{-2})**	**AIE (mWm^{-2})**	**Net aerosol forcing from ships in this scenario (mWm^{-2})**
BAU	-33.3	-31.1	-64.4
IMO scenario	-4.5	-14.6	-19.1
net change from BAU	+28.8	+16.5	+45.3
IMO + BC restriction scenario	-5.27 to -5.80	-14.6	-19.8 to -20.4
net change from BAU	+27.5 to +28.0	+16.5	+44.0 to +44.5
IMO + OC & BC restriction scenario	-5.08 to -5.60	-5.00	-10.1 to -10.6
net change from BAU	+28.2 to +27.7	+26.1	+53.8 to +54.3

Potential (AGWP) at a 100-year timescale for CO_2 is 92.5×10^{-15}yrWm^{-2} per kg CO_2 (Joos et al., 2013). From this, we can determine that on a 100-year timescale, ships have a global average radiative forcing of 84 mWm^{-2}. For each scenario, the required reduction of CO_2 is listed in Table 4.3. These restrictions range between half and two-thirds of all shipping CO_2.

Table 4.3: Reduction in CO_2 required to make each shipping scenario climate-neutral

Scenario	**CO_2 reduction required**
IMO scenario	Reduce shipping CO_2 emissions by 52%
IMO + BC restriction	Reduce shipping CO_2 emissions by 47%
IMO + BC + OC restriction	Reduce shipping CO_2 emissions by 64 - 65%

Chapter 5

Conclusions

We used GEOS-Chem to examine the radiative effects of several global shipping scenarios. These scenarios included the 'business as usual' (BAU) scenario, the IMO 2020 sulfur restriction scenario, and a new black and organic carbon restriction alongside with the IMO scenario. We used the TOMAS module to calculate particle mass and number distributions and the RRTMG module to calculate the aerosol direct and indirect effects based on these mass and number distributions. We also calculated the change in atmospheric concentrations due to these shipping scenarios. Finally, we calculated the reduction of ship-emitted carbon dioxide required to make each shipping scenario climate-neutral.

The simulations used the Community Emissions Data System (CEDS) and the NASA Aircraft and Satellites (ARCTAS) shipping emissions inventories. We examined the year 2013 and used meteorology and shipping activity data for that year to predict the effects of each scenarios. These simulations used a 4x5° resolution.

The direct radiative effect (DRE) of the BAU scenario is -64.4 mWm^{-2} and the aerosol indirect effect (AIE) is -31.1 mWm^{-2}. This leads to an overall radiative effect of -64.4 mWm^{-2}. Using this scenario as a baseline, the other scenarios have the following effects:

- The IMO scenario leads to 45.3 mWm^{-2} of increased warming
- The IMO + BC reduction scenario leads to 44.0 to 44.5 mWm^{-2} of increased

warming, depending on the mixing assumptions of BC

- The IMO + BC + OC reduction scenario leads to 53.8 to 54.3 mWm^{-2} of increased warming

The IMO + BC scenario leads to less warming than the IMO scenario. However, there is still an overall warming effect when SO_2 is reduced. The IMO + BC + OC reduction scenario leads to more warming than the IMO scenario. These results illustrate that black and organic compound reductions from ships is not an effective way to offset warming caused by the IMO 2020 sulfur restrictions. Other steps must be taken to reduce this warming, such as reducing CO_2 emissions. We determined that 47 - 65% of CO_2 emissions would have to be reduced from ships to make these scenarios climate-neutral.

Future Work

The results in this study assume shipping activity remains the same in 2020 as it was in 2013. However, shipping activity tends to increase most years, making these results a conservative estimate of the future. Furthermore, as Arctic sea ice continues to melt and open up new possible shipping routes, shipping in these areas will increase. Corbett et al. (2010) predicted 5% of global shipping traffic will switch to Arctic routes by 2050. Arctic shipping should be considered in future work, especially warming due to BC emissions in this high-albedo environment.

Future work should consider emissions over longer periods of time (multiple years or decades) and account for increased shipping activity with time. It should consider SECAs separately from the rest of the ocean, and conduct simulations at higher resolutions in order to better distinguish coastal areas where shipping emissions are very high. Online radiative transfer calculations should be considered to allow model chemistry to account for radiative effects.

Bibliography

H. Abdul-Razzak and S. J. Ghan. A parameterization of aerosol activation3. sectional representation. *JGR Atmospheres*, 107(D3), 2002. doi: 10.1029/2001JD000483.

P. J. Adams and J. H. Seinfeld. Predicting global aerosol size distributions in general circulation models. *JGR Atmospheres*, 107(D19):AAC 4–1–AAC 4–23, 2002. doi: 10.1029/2001JD001010.

Y. Balkanski, G. Myhre, M. Gauss, G. Rädel, E. J. Highwood, and K. P. Shine. Direct radiative effect of aerosols emitted by transport: from road, shipping and aviation. *Atmospheric Chemistry and Physics*, 10:4477–4489, 2010. doi: 10.5194/acp-10-4477-2010.

E. Baranizadeh, B. N. Murphy, J. Julin, S. Falahat, C. L. Reddington, A. Arola, L. Ahlm, S. Mikkonen, C. Fountoukis, D. Patoulias, A. Minikin, T. Hamburger, A. Laaksonen, S. N. Pandis, H. Vehkamäki, K. E. J. Lehtinen, and I. Riipinen. Implementation of state-of-the-art ternary new-particle formation scheme to the regional chemical transport model pmcamx-uf in europe. *Geoscientific Model Development*, 9:2741–2754, 2016. doi: 10.5194/gmd-9-2741-2016.

H. W. Barker, J. N. S. Cole, J. Morcrette, R. Pincus, P. Räisänen, K. von Salzen, and P. A. Vaillancourt. The monte carlo independent column approximation: an assessment using several global atmospheric models. *Quarterly Journal of the Royal Meteorological Society*, 134(635):1463–1478, 2008. doi: 10.1002/qj.303.

E. K. Berner and R. A. Berner. *Global Environment: Water, Air, and Geochemical Cycles*. Princeton University Press, Princeton, New Jersey, 2012.

I. Bey, D. J. Jacob, R. M. Yantosca, J. A. Logan, B. D. Field, A. M. Fiore, Q. Li, H. Y. Liu, L. J. Mickley, and M. G. Schultz. Global modeling of tropospheric chemistry with assimilated meteorology: Model description and evaluation. *JGR Atmospheres*, 206(D19):23073–23095, 2001. doi: 10.1029/2001JD000807.

C. F. Bohren and D. R. Huffman. *Absorption and Scattering of Light by Small Particles*. Wiley, New York, New York, 1983.

T. C. Bond and R. W. Bergstrom. Light absorption by carbonaceous particles: An investigative review. *Aerosol Science and Technology*, 40(1):27–67, 2006. doi: 10.1080/02786820500421521.

T. C. Bond, D. G. Streets, K. F. Yarber, S. M. Nelson, J.-H. Woo, and Z. Klimont. A technology-based global inventory of black and organic carbon emissions from combustion. *JGR Atmospheres*, 109(D14), 2004. doi: 10.1029/2003JD003697.

M. A. Box and G. P. Box. *Physics of Radiation and Climate*. CRC Press, Boca Raton, Florida, 2016.

G. P. Brasseur and E. Roeckner. Impact of improved air quality on the future evolution of climate. *Geophysical Research Letters*, 32(23), 2005. doi: 10.1029/2005GL023902.

G. P. Brasseur, J. J. Orlando, and G. S. Tyndall. *Atmospheric Chemistry and Global Change*. Oxford University Press, New York, New York, 1999.

K. Chance and R. V. Martin. *Spectroscopy Radiative Transfer of Planetary Atmospheres*. Oxford University Press, New York, New York, 2017.

K. K. Chandrakar, W. Cantrell, and R. A. Shaw. Influence of turbulent fluctuations on cloud droplet size dispersion and aerosol indirect effects. *American Meteorological Society*, 79:3191–3209, 2018. doi: 10.1175/JAS-D-18-0006.1.

R. Cherian, J. Quaas, M. Salzmann, and L. Tomassini. Black carbon indirect radiative effects in a climate model. *Tellus B: Chemical and Physical Meteorology*, 69(1), 2017. doi: http://creativecommons.org/licenses/by/4.0/.

S. A. Clough, M. W. Shephard, E. J. Mlawer, J. S. Delamere, M. J. Iacono, K. Cady-Pereira, S. Boukabara, and P. D. Brown. Atmospheric radiative transfer modeling: a summary of the aer codes. *Journal of Quantitative Spectroscopy and Radiative Transfer*, 91(2):233–244, 2005. doi: 10.1016/j.jqsrt.2004.05.058.

B. Comer, N. Olmer, X. Mao, B. Roy, and D. Rutherford. Prevalence of heavy fuel oil and black carbon in Arctic shipping, 2015 to 2025. Technical report, 2017.

J. Corbett, J. Winebrake, and E. Green. An assessment of technologies for reducing regional short-lived climate forcers emitted by ships with implications for arctic shipping. *Carbon Management*, 1(2):207–225, 2010. doi: 10.4155/cmt.10.27.

B. Croft, R. V. Martin, W. R. Leaitch, P. Tunved, T. J. Breider, S. D. D'Andrea, and J. R. Pierce. Processes controlling the annual cycle of arctic aerosol number and size distributions. *Atmospheric Chemistry and Physics*, 16:3665–3682, 2016. doi: 10.5194/acp-16-3665-2016.

B. Croft, R. V. Martin, W. R. Leaitch, J. Burkart, R. Y. Chang, D. B. Collins, P. L. Hayes, A. L. Hodshire, L. Huang, J. K. Kodros, A. Moravek, E. L. Mungall, J. G. Murphy, S. Sharma, S. Tremblay, G. R. Wentworth, and M. D. Willis. Arctic marine secondary organic aerosol contributes significantly to summertime particle size distributions in the canadian arctic archipelago. *Atmospheric Chemistry and Physics*, 19:2787–2812, 2019. doi: 10.5194/acp-19-2787-2019.

A. Dosio, L. Mentaschi, E. M. Fischer, and K. Wyser. Extreme heat waves under 1.5 c and 2 c global warming. *Environmental Research Letters*, 13(5):054006, 2018.

S. D. Eastham, D. K. Weisenstein, and S. R. Barretta. Development and evaluation of the unified troposphericestratosphericchemistry extension (ucx) for the global chemistry-transport modelgeos-chem. *Atmospheric Environment*, 89:52–63, 2014. doi: 10.1016/j.atmosenv.2014.02.001.

V. Eyring, H. W. Köhler, J. van Aardenne, and A. Lauer. Emissions from international shipping: 1. the last 50 years. *JGR Atmospheres*, 110(D17), 2005. doi: https://doi:10.1029/2004JD005619.

K. Fagerholt, N. T. Gausel, J. G. Rakke, and H. N. Psaraftis. Maritime routing and speed optimization with emission control areas. *Transportation Research Part C: Emerging Technologies*, 52:57 – 73, 2015. ISSN 0968-090X. doi: 10.1016/j.trc.2014.12.010.

G. Feingold, S. M. Kreidenweis, and B. S. W. R. Cotton. Numerical simulations of stratocumulus processing of cloud condensation nuclei through collision-coalescence. *JGR: Atmospheres*, 101(D16):21183–21437, 1996. doi: 10.1029/96JD01552.

Q. Fu and K. N. Liou. On the correlated k-distribution method for radiative transfer in nonhomogenous atmospheres. *Journal of the Atmospheric Sciences*, 49(22): 2139–2156, 1992. doi: 10.1175/1520-0469.

N. A. Fuchs, R. E. Daisley, M. Fuchs, C. N. Davies, and M. E. Straumanis. The mechanics of aerosols. *Physics Today*, 18(4):73, 1965. doi: 10.1063/1.3047354.

J. Fuglestvedt, T. Berntsen, G. Myhre, K. Rypdal, and R. B. Skeie. Climate forcing from the transport sectors. *Proceedings of the National Academy of Sciences of the United States of America*, 105(2):454–458, 2008. doi: 10.1073/pnas.0702958104.

G. B. Hamra, N. Guha, A. Cohen, F. Laden, O. Raaschou-Nielsen, J. M. Samet, P. Vineis, F. Forastiere, P. Saldiva, T. Yorifuji, and D. Loomis. Outdoor particulate matter exposure and lung cancer: A systematic review and meta-analysis. *Environmental Health Perspectives*, 22(9), 2014. doi: 10.1289/ehp/1408092.

C. L. Heald, D. A. Ridley, J. H. Kroll, S. R. H. Barrett, K. E. Cady-Pereira, M. J. Alvarado, and C. D. Holmes. Contrasting the direct radiative effect and direct radiative forcing of aerosols. *Atmospheric Chemistry and Physics*, 14(11):5513–5527, 2014. doi: 10.5194/acp-14-5513-2014.

P. V. Hobbs. *Aerosol-Cloud-Climate Interactions*. Academic Press Inc., San Diego, California, 1993.

R. M. Hoesly, S. J. Smith, L. Feng, Z. Klimont, G. Janssens-Maenhout, T. Pitkanen, J. J. Seibert, L. Vu, R. J. Andres, R. M. Bolt, T. C. Bond, L. Dawidowski, N. Kholod, J.-I. Kurokawa, M. Li, L. Liu, Z. Lu, M. C. P. Moura, P. R. O'Rourke, and Q. Zhang. Historical (1750–2014) anthropogenic emissions of reactive gases and aerosols from the community emissions data system (ceds). *Geoscientific Model Development*, 11:369–408, 2018. doi: 10.5194/gmd-11-369-2018.

J. Houghton. *Global Warming: The Complete Briefing*. Cambridge University Press, Cabridge, United Kingdom, 2015.

M. J. Iacono, J. S. Delamere, E. J. Mlawer, Mark, W. Shephard, S. A. Clough, and W. D. Collins. Radiative forcing by long-lived greenhouse gases: Calculations with the aer radiative transfer models. *JGR Atmospheres*, 113(D13), 2008. doi: 10.1029/2008JD009944.

International Maritime Organization. Investigation of Appropriate Control Measures (Abatement Techonologies) to Reduce Black Carbon Emissions from International Shipping. Technical report, 2015.

D. Jacob. *Introduction to Atmospheric Chemistry*. Princeton University Press, Princeton, New Jersey, 1999.

L. Johansson, J. P. Jalkanen, and J. Kukkonen. Global assessment of shipping emissions in 2015 on a high spatial and temporal resolution. *Atmospheric Environment*, 167:403–415, 2017. doi: 10.1016/j.atmosenv.2017.08.042.

F. Joos, R. Roth, J. S. Fuglestvedt, G. P. Peters, I. G. Enting, W. von Bloh, V. Brovkin, E. J. Burke, M. Eby, N. R. Edwards, T. Friedrich, T. L. Frölicher, P. R. Halloran, P. B. Holden, C. Jones, T. Kleinen, F. T. Mackenzie, K. Matsumoto, M. Meinshausen, G.-K. Plattner, A. Reisinger, J. Segschneider, G. Shaffer, M. Steinacher, K. Strassmann, K. Tanaka, A. Timmermann, and A. J. Weaver. Carbon dioxide and climate impulse response functions for the computation of greenhouse gas metrics: a multi-model analysis. *Atmospheric Chemistry and Physics*, 13(5):2793–2825, 2013.

C. A. Keller, M. S. Long, R. M. Yantosca, A. M. D. Silva, S. Pawson, and D. J. Jacob. Hemco v1.0: a versatile, esmf-compliant component for calculating emissions in atmospheric models. *Geoscientific Model Development*, 7:1409–1417, 2014. doi: https://doi:10.5194/gmd-7-1409-2014.

K.-H. Kim, E. Kabir, and S. Kabir. A review on the human health impact of airborne particulate matter. *Environment International*, 74:136–143, 2015. doi: 10.1016/j.envint.2014.10.005.

Z. Klimont, K. Kupiainen, C. Heyes, P. Purohit, J. Cofala, P. Rafaj, J. Borken-Kleefeld1, and W. Schöpp. Supplement of global anthropogenic emissions of particulate matter including black carbon. *Atmospheric Chemistry and Physics*, 17: 8681–8723, 2017. doi: 10.5194/acp-17-8681-2017.

J. K. Kodros, R. Cucinotta, D. A. Ridley, C. Wiedinmyer, and J. R. Pierce. The

aerosol radiative effects of uncontrolled combustionof domestic waste. *Atmospheric Chemistry and Physics*, 16:6771–6784, 2016. doi: 10.5194/acp-16-6771-2016.

J. K. Kodros, A. K. Hanna, Sarah J.and Bertram, W. Richard Leaitch, H. Schulz, A. B. Herber, M. Zanatta, J. Burkart, Willis, M. D., J. P. Abbatt, and J. R. Pierce. Size-resolved mixing state of black carbon in the canadian high arctic and implications for simulated direct radiative effect. *Atmospheric Chemistry and Physics*, 18(15):11345–11361, 2018. doi: 10.5194/acp-18-11345-2018.

P. Koepke, M. Hess, I. Schult, and E. P. Shettle. Global aerosol dataset, mpi meteorologie hamburg report no. 243. page 44, 1997.

D. A. Lack and J. J. Corbett. Black carbon from ships: A review of the effects of ship speed, fuel quality and exhaust gas scrubbing. *Atmospheric Chemistry and Physics*, 12(9):3985–4000, 2012. doi: 10.5194/acp-12-3985-2012.

A. Lauer, V. Eyring, J. J. Corbett, C. F. Wang, and J. J. Winebrake. Assessment of near-future policy instruments for oceangoing shipping: impact on atmospheric aerosol burdens and the earth's radiation budget. *Environmental Science Technology*, 43:5592–5598, 2009. doi: 10.1021/es900922h.

G. Lesins, P. Chylek, and U. Lohmann. A study of internal and external mixing scenarios and its effect on aerosol optical properties and direct radiative forcing. *JGR Atmospheres*, 107(D10):AAC 5–1–AAC 5–12, 2002. doi: 10.1029/2001JD000973.

M. Lund, V. Eyring, J. Fuglestvedt, J. Hendricks, A. Lauer, D. Lee, and M. Righi. Global-mean temperature change from shipping toward 2050: improved representation of the indirect aerosol effect in simple climate models. *Environmental Science Technology*, 46:8868–8877, 2012. doi: 10.1021/es301166e.

J. Löndahl, A. Massling, J. Pagels, E. Swietlicki, and E. Vaclavik. Size-resolved respiratory-tract deposition of fine and ultrafine hydrophobic and hygroscopic

aerosol particles during rest and exercise. *Inhalation Toxicology*, 19(2):109–116, 2007. doi: 10.1080/08958370601051677.

Z. Meng and Y. Liu. Cell morphological ultrastructural changes in various organs from mice exposed by inhalation to sulfur dioxide. *Inhalation Toxicology*, 19(6-7): 543–551, 2007. doi: 10.1080/08958370701271373.

N. Olmer, B. Comer, B. Roy, X. Mao, and D. Rutherford. Greenhouse Gas Emissions from Global Shipping 2013 - 2015. Technical report, 2017.

L. Oreopoulos, R. F. Cahalan, and S. Platnick. The plane-parallel albedo bias of liquid clouds from modis observations. *Journal of Climate*, 32(7), 2007. doi: 10.1175/JCLI4305.1.

R. Pachauri and L. Meyer. Climate Change 2014: Synthesis Report. Contribution of Working Groups I, II and III to the Fifth Assessment Report of the Intergovernmental Panel on Climate Change. Technical report, 2014.

A. I. Partanen, A. Laakso, A. Schmidt, H. Kokkola, T. Kuokkanen, J.-P. Pietikäinen, V.-M. Kerminen, K. E. J. Lehtinen, L. Laakso, and H. Korhonen. Climate and air quality trade-offs in altering ship fuel sulfur content. *Atmospheric Chemistry and Physics*, 13:12059–12071, 2013. doi: doi:10.5194/acp-13-12059-2013.

S. Pawson. Geos systems, 2017. `https://gmao.gsfc.nasa.gov/GEOS_systems/` [Accessed: February 2019].

H. Pham and T. Nguyen. Solution to reduce air environmental pollution from ships. *International Journal on Marine Navigation and Safety of Sea Transportation*, 9 (2):257–261, 2017. doi: http://doi.org/10.12716/1001.09.02.14.

R. Pincus, H. W. Barker, and J. Morcrette. A fast, flexible, approximate technique

for computing radiative transfer in inhomogeneous cloud fields. *JGR Atmospheres*, 108(D13), 2003. doi: 10.1029/2002JD003322.

M. V. Ramana, V. Ramanathan, Y. Feng, S. C. Yoon, S. W. Kim, and J. J. Carmichael, G. R. Schauer. Warming influenced by the ratio of black carbon to sulphate and the black-carbon source. *Nature Geoscience*, 3(8):542–545, 2010. doi: 10.1038/ngeo918.

C. E. Scott, A. Rap, D. V. Spracklen, P. M. Forster, K. S. Carslaw, G. W. Mann, K. J. Pringle, N. Kivekäs, M. Kulmala, H. Lihavainen, and P. Tunved. The direct and indirect radiative effects of biogenic secondary organic aerosol. *Atmospheric Chemistry and Physics*, 14:447–470, 2014. doi: 10.5194/acp-14-447-2014.

J. Soares, C. Geels, , J. Langner, S. Tsyro, A. Kurganskiy, J. Ström, J. Gallet, M. Ruppel, and M. So. *Air Pollution Modeling and its Application XXV*. Springer International Publishing, 2018. doi: 10.1007/978-3-319-57645-9.

M. Sofiev, J. J. Winebrake, L. Johansson, E. W. Carr, M. Prank, J. Soares, J. Vira, R. Kouznetsov, J. P. Jalkanen, and J. J. Corbett. Cleaner fuels for ships provide public health benefits with climate tradeoffs. *Nature Communications*, 9(1):1–12, 2018. doi: 10.1038/s41467-017-02774-9.

B. Stiller, T. Bocek, F. Hecht, G. Machado, P. Racz, and M. Waldburger. Health effects of black carbon. Technical report, WHO Regional Office for Europe, 2012.

C. Tomasi, S. Fuzzi, and A. Kokhanovsky. *Atmospheric Aerosols: Life Cycles and Effects on Air Quality and Climate*. Wiley-VCH Verlag GmbH Co. KGaA, Weinheim, Germany, 2017.

UN-Business Action Hub. Imo profile. https://business.un.org/en/entities/13.

US EPA. Radiative forcing caused by human activities since 1750, 2014. URL https://www.epa.gov/climate-indicators/climate-change-indicators-climate-forcing. [Online; accessed April 2, 2019].

T. R. Walker, O. Adebambo, M. C. D. A. Feijoo, E. Elhaimer, T. Hossain, S. J. Edwards, C. E. Morrison, J. Romo, N. Sharma, S. Taylor, and S. Zomorodi. *World Seas: An Environmental Evaluation - Chapter 30: Environmental Effects of Marine Transportation.* Academic Press, Cambridge, Massachusetts, 2018.

M. L. Wesley. Parameterization of surface resistances to gaseous dry deposition in regional-scale numerical models. *Atmospheric Environment*, 23:1293–1304, 1989.

World Health Organization. Ambient (outdoor) air quality and health, 2018. https://www.who.int/en/news-room/fact-sheets/detail/ambient-(outdoor)-air-quality-and-health.